Check for updates

Received: 8 September 2021 | Revised: 9 February 2022 | Accepted: 23 April 2022

DOI: 10.1002/fld.5116

RESEARCH ARTICLE

WILEY

A time-staggered second order conservative time scheme for variable density flow

Hector Amino[1,2] | **Cédric Flageul**[3] | **Sofiane Benhamadouche**[1,2] | **Iztok Tiselj**[4] | **Bertrand Carissimo**[1,2] | **Martin Ferrand**[1,2]

[1]Fluid Mechanics, Energy and Environment Department, EDF R&D, Chatou, France

[2]CEREA, Ecole des Ponts, EDF R&D, Chatou, France

[3]PPRIME Institute, Curiosity Group, Université de Poitiers, CNRS, ISAE-ENSMA, France

[4]Reactor Engineering Division, Jožef Stefan Institute, Ljubljana, Slovenia

Correspondence
Martin Ferrand and Hector Amino, Fluid Mechanics, Energy and Environment Department, EDF R&D, Chatou, France.
Email: hector.galante-amino@edf.fr and martin.ferrand@edf.fr

Abstract

In this study, we present a robust conservative time-staggered scheme for variable density flow. This pressure correction scheme uses the compressible Navier–Stokes equations and is implemented in the collocated finite-volume open-source computational fluid dynamics solver code_saturne. The Helmholtz equation is solved for the pressure increment, taking the thermodynamic pressure into account and avoiding the acoustic time step limitation. The internal energy equation is used and completed by a source term derived from the discrete kinetic energy equation, thus enforcing total energy conservation and consistency for irregular solutions. A numerical analysis providing conditions ensuring the positivity of the thermodynamic variables is proposed. The scheme is verified and validated against analytical and experimental test cases. Its ability to reproduce the pressure variation while conserving the mass is demonstrated. Its conservative property and time convergence order are also verified. An irregular shock solution is studied, emphasizing the importance of the source term in the internal energy equation. Finally, the scheme is validated against reference numerical results on a two-dimensional natural convection cavity and experimental data on a three-dimensional ventilation test case. The comparison against experimental data is made using first-and second-order turbulent simulations.

KEYWORDS

CFD, pressure correction, finite volume, compressible flow, second order, RANS, LES

1 | INTRODUCTION

Simulating variable density flow at all Mach numbers is an active field of research and is useful in many industrial domains such as combustion,[1] indoor air flow,[2] and power generation industries.[3,4] When the flow Mach number tends to zero, the compressible Navier–Stokes equations converge toward the incompressible ones.[5] This is not easily achieved in numerical simulations as an incompressible formulation of the equations does not reproduce well compressible effects and compressible solvers can perform poorly when the Mach number decreases.[6] In the latter context, the low-Mach set of the Navier–Stokes equations are often used to describe flow motion, where the acoustic waves propagate at an infinite speed and are not considered in the simulation. Nevertheless, if one wants to consider its effects on the flow, the compressible

This is an open access article under the terms of the Creative Commons Attribution License, which permits use, distribution and reproduction in any medium, provided the original work is properly cited.
© 2022 The Authors. *International Journal for Numerical Methods in Fluids* published by John Wiley & Sons, Ltd.

Navier–Stokes equations are used. In this case, an additional numerical constraint appears, limiting the simulation time step related to sound celerity. This can be very inconvenient for slow-speed flow simulations. Thus, significant attention was given to designing time schemes for computational fluid dynamics (CFD) able to cover both regimes, while compromising the preservation of accurate numerical results and reducing the total computational calculation time. In that scope, one solution is the use of implicit time integrators, which may not be simple to implement due to the complexity of the system to solve. An alternative method related to different time scale problems is the implicit treatment of some terms of the system while keeping the remaining explicit. This semi implicit (or implicit explicit) approach allows the development of stabler schemes by reducing the time step constraint related to the fast time scale. In the context of incompressible and compressible flow, different all speed semi-implicit schemes based on the asymptotic preserving method have been proposed in the last decades,[7-11] which inspired some features of the presented scheme, notably the incompressible limit of the pressure equation. Moreover, the present scheme belongs to the pressure correction methods, which are time marching techniques widely used in CFD. First introduced in the late 60's[12,13] for incompressible flow (see Reference 14 for a review of the different variants), they were extended for compressible flow[15,16] followed by many numerical schemes, mostly using finite volume methods. Among them, one can highlight the essentially implicit[17-20] algorithms which differ from the semi-implicit ones (such as the SIMPLE[21] method and its derivatives) where a prediction of the momentum is first performed, followed by a correction step for the pressure, momentum, and velocity.[22-26] Furthermore, several recent work addressed a strategy of using high-order schemes to capture unsteady turbulent flow phenomena. In 1965, Harlow and Welch[27] introduced a staggered grid arrangement for a second-order finite-difference scheme for incompressible flow using the Crank–Nicolson scheme.[28] Pierce and Moin[29] extended the previous scheme to variable-density flow using the low Mach assumption. An extended version of this algorithm was proposed by the same authors,[30] where a Helmholtz equation was used instead of a Poisson equation in the correction step, avoiding the acoustic Courant–Friedrichs–Lewy (CFL) number limitation. The latter used the enthalpy equation to compute the temperature and was specially designed for low speed flow, with no presence of shocks. Solving a Helmholtz equation to correct the pressure was also shown to be relevant for an atmospheric flow solver by Benacchio and Klein[31] and for a low Mach number kinetic energy conservation scheme by Moureau et al.[32] High-order low and all Mach number schemes remain very popular. Desjardins et al.[33] proposed a high order version of Pierce's low Mach finite differences staggered time-stepping, using the Poisson equation in the correction step. The combination of semi-implicit asymptotic preserving and Runge–Kutta methods[34-36] led also to high-order all Mach number schemes.[10,37] Note that boundary conditions, specially in incompressible pressure correction methods, can affect its time convergence order.[14] This is beyond the scope of the current study.

In this manuscript, we present a conservative second-order time scheme for variable density flow using the compressible Navier–Stokes equations. The finite difference scheme introduced by Pierce and Moin[29] with a staggered variable arrangement in time is extended on different grounds using the collocated finite-volume discretization[38] for regular and discontinuous solutions. Three major features of the new scheme are highlighted. First, it includes the effect of the thermodynamic pressure in the correction step by solving a Helmholtz equation. Therefore, the acoustic waves are treated implicitly and are thus separated from advection, which removes the acoustic CFL restriction on the time step. Moreover, the internal energy equation is used to compute the temperature. First introduced by Herbin et al.[26] for an Euler pressure correction scheme, this choice of equation allows the third feature, a numerical analysis, to be made, ensuring the temperature, pressure and density positivity under certain constraints detailed later. Since computing shock solutions using the internal energy equation yields an incorrect velocity field,[3,39] a correction term based on the discrete kinetic energy equation similar to that used by Herbin et al.[26] is added to the internal energy equation. This term, derived here for the sub-iterative time-staggered scheme, preserves the sum of the internal and kinetic energy to ensure the conservation of the total energy, thus implying a good reproducibility of the numerical shock velocities.

The proposed algorithm, from now on called compressible pressure correction (CPC) scheme, is implemented in the open-source CFD solver code_saturne,[40] which is used extensively in the industry for nuclear thermal-hydraulic applications,[41] atmospheric modeling,[42,43] ventilation, wave interactions,[44] and combustion.[45]

The remainder of this paper is organized as follows. We first introduce the set of the continuous equations and turbulence models used. The discrete spatial and temporal schemes are then described and a numerical analysis to ensure the thermodynamic fields positivity is performed. Finally, the CPC scheme properties are verified on analytical test cases and their numerical results are compared with the existing code_saturneincompressible second-order variable density (incompressible pressure correction (IPC)) time scheme for reactive flow, by Ma et al.[46] and compressible scheme by Colas et al.,[47] which uses an isentropic pressure correction step. This is first done with a pressure-cooker-like system, showing that the scheme takes into account the correct pressure variation while preserving the systems' global mass, and then by transporting a scalar through an one-dimensional tube in order to verify both mass and momentum conservation and the

10970363, 2022, 12, Downloaded from https://onlinelibrary.wiley.com/doi/10.1002/fld.5116 by Jozef Stefan Institute, Wiley Online Library on [07/04/2025]. See the Terms and Conditions (https://onlinelibrary.wiley.com/terms-and-conditions) on Wiley Online Library for rules of use; OA articles are governed by the applicable Creative Commons License

time scheme convergence order. Its consistency related to irregular solutions is then tested with a shock tube configuration. Finally, the model is validated on a natural convection and a ventilation case, emphasizing the presented scheme's ability and robustness to provide accurate results in the industrial context.

2 | GOVERNING EQUATIONS AND TIME SCHEME

2.1 | Governing equations

Fluid motion, when studied with the continuum hypothesis in a bounded space Ω, is described by the Navier–Stokes compressible equations supplemented with scalars Y transport equations and an equation of state. Considering an ideal gas of density ρ, velocity $\underline{u}$, momentum $\underline{q} \coloneqq \rho\underline{u}$, internal energy e, temperature T, viscosity μ, heat capacities c_v and c_p, thermal conductivity λ, and scalar diffusion coefficient K, the equations read:

$$
\begin{aligned}
&(a)\ \ \frac{\partial \rho}{\partial t} + \operatorname{div}\left(\underline{q}\right) = 0,\\
&(b)\ \ \frac{\partial \underline{q}}{\partial t} + \underline{\operatorname{div}}\left(\underline{u}\otimes\underline{q}\right) = -\underline{\nabla} p + \underline{\operatorname{div}}\left(\underline{\underline{\tau}}\right) + \underline{f},\\
&(c)\ \ \frac{\partial (\rho\ e)}{\partial t} + \operatorname{div}\left(e\underline{q}\right) = -p\operatorname{div}\left(\underline{u}\right) + \underline{\underline{\tau}} : \underline{\underline{\nabla u}} + \operatorname{div}\left(\lambda\underline{\nabla} T\right),\\
&(d)\ \ \frac{\partial (\rho\ Y)}{\partial t} + \operatorname{div}\left(Y\underline{q}\right) = \operatorname{div}\left(K\underline{\nabla} Y\right),\\
&(e)\ \ T = \mathcal{T}(\rho, e) = \frac{\gamma - 1}{R_a}\, e, \qquad p = \mathcal{P}(\rho, e) = \rho R_a T.
\end{aligned}
\tag{1}
$$

$\underline{f}$ is the field of volume force (*e.g.* gravity force $\rho\underline{g}$), $\underline{\underline{\tau}} = \mu\left(\underline{\underline{\nabla}}\,\underline{u} + \underline{\underline{\nabla}}\,\underline{u}^T\right) + \left(\kappa - \frac{2}{3}\mu\right)\operatorname{div}(\underline{u})\underline{\underline{I}}$, is the shear stress tensor. κ is the volume viscosity, which is usually neglected and is therefore omitted hereafter in this article. $\gamma = c_p/c_v$ is the fluid heat capacity ratio, and $R_a = R/M_a$ is the specific gas constant. Possible additional source terms were not considered in the aforementioned equations.

2.2 | Turbulence modeling

Two turbulence approaches are used in this study. The first is the Reynolds Averaged Navier–Stokes equations (RANS) which decomposes the fluid variables into a mean and a fluctuating part using the Reynolds average operator $\overline{(.)}$. A flow variable ψ is written as $\psi = \overline{\psi} + \psi'$. For compressible and low compressible flow, the density weighted Favre average operator is used instead (i.e., $\tilde{\psi} = \overline{\rho\psi}/\overline{\rho}$, $\psi = \tilde{\psi} + \psi''$).

The second approach is the large eddy simulation (LES), where a spatial filter is applied on the Navier Stokes equations; one part of the turbulence spectrum is solved whereas the other is modeled. ψ being a variable, the filtering operation $\overline{\psi}$ is defined as $\overline{\psi} = \int_{-\infty}^{\infty} G(x-\xi)\psi(\xi)d\xi$, where G is the LES filter function. Similar to the RANS method, the Favre filter is defined as $\tilde{\psi} = \overline{\rho\psi}/\overline{\rho}$. For both turbulent approaches, the averaged Navier–Stokes equations read:

$$
\begin{aligned}
&(a)\ \ \frac{\partial \overline{\rho}}{\partial t} + \operatorname{div}\left(\overline{\underline{q}}\right) = 0,\\
&(b)\ \ \frac{\partial \overline{\underline{q}}}{\partial t} + \underline{\operatorname{div}}\left(\tilde{\underline{u}}\otimes\overline{\underline{q}}\right) = -\underline{\nabla}\overline{p} + \underline{\operatorname{div}}\left(\mu\left[\underline{\underline{\nabla}}\tilde{\underline{u}} + \underline{\underline{\nabla}}\tilde{\underline{u}}^T - \frac{2}{3}\operatorname{div}\tilde{\underline{u}}\ \underline{\underline{I}}\right]\right) - \underline{\operatorname{div}}\left(\underline{\underline{\tau}}_T\right) + \overline{\underline{f}},\\
&(c)\ \ \frac{\partial\left(\overline{\rho}\ \tilde{e}\right)}{\partial t} + \operatorname{div}\left(\tilde{e}\otimes\overline{\underline{q}}\right) = -\overline{p}\operatorname{div}\left(\tilde{\underline{u}}\right) + \operatorname{div}\left(\lambda\underline{\nabla}\tilde{T}\right) + \underbrace{\operatorname{div}\left(\lambda\underline{\nabla}\overline{T''}\right)}_{(1*)}\\
&\qquad - c_v\operatorname{div}\left(\overline{\rho}\,\overline{\underline{u}''T''}\right) + \underline{\underline{\tilde{\tau}}} : \underline{\underline{\nabla}}\tilde{\underline{u}} + \underbrace{\overline{\underline{\underline{\tau}} : \underline{\underline{\nabla u''}}}}_{(2*)} + \underbrace{\overline{\underline{\underline{\tau''}} : \underline{\underline{\nabla}}\tilde{\underline{u}}}}_{(3*)},\\
&(d)\ \ \frac{\partial\left(\overline{\rho}\ \tilde{Y}\right)}{\partial t} + \operatorname{div}\left(\tilde{Y}\otimes\overline{\underline{q}}\right) = \operatorname{div}\left(K\underline{\nabla}\tilde{Y}\right) + \operatorname{div}\left(K\underline{\nabla}\overline{Y''}\right),\\
&(e)\ \ \overline{p} = \overline{\rho}R_a\tilde{T},
\end{aligned}
\tag{2}
$$

10970363, 2022, 12, Downloaded from https://onlinelibrary.wiley.com/doi/10.1002/fld.5116 by Jozef Stefan Institute, Wiley Online Library on [07/04/2025]. See the Terms and Conditions (https://onlinelibrary.wiley.com/terms-and-conditions) on Wiley Online Library for rules of use; OA articles are governed by the applicable Creative Commons License

where $\overline{\underline{q}} = \overline{\rho}\overline{\underline{\tilde{u}}}$ and $\overline{\underline{f}}$ is the source term. The term (1*) can be neglected considering $\Delta\tilde{T} >> \Delta T''$, which is true for nearly all flows. The same is considered for the scalar transport equation. Terms (2*) and (3*) can also be neglected by assuming a flow below the hypersonic regime and that $|\overline{\underline{\tilde{\tau}}}| >> |\overline{\underline{\tau}}''|$. The tensor $\underline{\underline{\tau}}_T$ is defined according to the operator applied to the balance equations. For the RANS approach, $\underline{\underline{\tau}}_T = \overline{\rho}\underline{\underline{R}}$, with $\underline{\underline{R}} = \overline{\rho u_i'' u_j''}/\overline{\rho}$ being the Reynolds stress tensor. If the filter operator is used, $\underline{\underline{\tau}}_T$ is the subgrid stress tensor defined as $\underline{\underline{\tau}}^{sgs} := \overline{\rho}(\widetilde{u_i u_j} - \tilde{u}_i\tilde{u}_j)$. In both RANS and LES simulations, a closure for $\underline{\underline{\tau}}_T$ is required. The averaged temperature equation also presents a new term corresponding to the turbulent heat flux $\overline{\underline{u}''T''}$ which also requires a closure (e.g., the simple gradient diffusion hypothesis or the generalized gradient diffusion hypothesis).

In the present study, RANS calculations were computed using the $k-\varepsilon$[48] model or differential Reynolds stress models (DRAM). The first is an eddy viscosity model, which transports the turbulent kinetic energy k and its dissipation rate ε over the flow. The second model solves the Reynolds stress tensor $\underline{\underline{R}}$ transport equations. In the latter, the following closures are used: the Shir model[49] is used to close the Reynolds stress tensor equation turbulent diffusive term, and the SSG[50] closure is used to model the velocity-pressure gradient correlation. Finally, the dynamic Smagorinsky model[51] was used to close the LES equations, completed with Lilly's[52] minimization resolution. For the sake of simplicity, equations are written without the average and filter operators from now on.

2.3 | Space and time discretization

The space domain Ω is meshed with a collection of polyhedral cells c of volume Ω_c. Two neighboring cells c and $\tilde{c}$ share a polygonal face f of the normal surface vector $\underline{S}_f$ oriented from c to $\tilde{c}$, as shown in Figure 1.

Mean space values over a cell Ω_c and averaged values over a face f of $(.)$ are denoted by:

$$(.)_c := \frac{1}{\Omega_c}\int_c (.)\mathrm{d}\Omega, \qquad (.)_f := \frac{1}{S_f}\int_f (.)\mathrm{d}S. \tag{3}$$

S_f is the cell measure and the surface. Note that face values are computed using special schemes, which are beyond the scope of this work (see[40] for more details). The mean time value over the time interval $[t^n,\ t^{n+1}]$ is denoted by

$$(.)|_n^{n+1} := \frac{1}{\Delta t}\int_{t^n}^{t^{n+1}} (.)\mathrm{d}t, \tag{4}$$

where Δt is the interval measure. Moreover, the time values at time t^n and t^{n+1} are written with the superscript $(.)^n$ and $(.)^{n+1}$, respectively. The time interval $\Delta t|_n^{n+1}$ is then $t^{n+1} - t^n$.

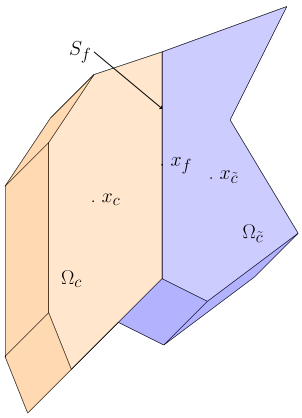

FIGURE 1 Labeling information used for a mesh. x_c and $x_{\tilde{c}}$ are the barycenters of cells c and $\tilde{c}$, respectively. x_f is the barycenter of the face f separating the two cells. [Colour figure can be viewed at wileyonlinelibrary.com]

10970363, 2022, 12, Downloaded from https://onlinelibrary.wiley.com/doi/10.1002/fld.5116 by Jozef Stefan Institute, Wiley Online Library on [07/04/2025]. See the Terms and Conditions (https://onlinelibrary.wiley.com/terms-and-conditions) on Wiley Online Library for rules of use; OA articles are governed by the applicable Creative Commons License

In the present numerical scheme, the time stepping is defined by the parameter θ, bounded in $[0,1]$. We consider the cases where $\theta = 1$ (implicit Euler, 1st order time interpolation of $(.)|_n^{n+1}$) and $\theta = 1/2$ (Crank Nicolson, 2nd order time interpolation of $(.)|_n^{n+1}$). A field ψ time interpolation $\Theta\left(\psi^n, \psi^{n+1}\right)$ between times n and $n+1$ is defined as:

$$\Theta\left(\psi^n, \psi^{n+1}\right) \coloneqq (1-\theta)\,\psi^n + \theta\psi^{n+1}.$$

The dual time interval around time n is denoted by $[n-1+\theta, n+\theta]$, and is of length:

$$\Delta t|_{n-1+\theta}^{n+\theta} \coloneqq \Theta\left(\Delta t|_{n-1}^{n},\ \Delta t|_n^{n+1}\right),$$

From the above expressions, the extensive quantities such as the cell mass M_c, cell momentum $\underline{Q}_c$ and face mass flux $\dot{M}_f$ are defined as follows:

$$M_c \coloneqq \int_c \rho \mathrm{d}\Omega, \qquad \underline{Q}_c \coloneqq \int_c \rho \underline{u} \mathrm{d}\Omega, \qquad \dot{M}_f \coloneqq \int_f \underline{q} \cdot \underline{dS} = \underline{q}_f \cdot \underline{S}_f.$$

Finally, discrete spatial operators (denoted by capital letters) are defined. The discrete operator divergence of a face-averaged field $\underline{\psi}_f$ is as follows:

$$\mathrm{Div}_c\left(\underline{\psi}_f\right) \coloneqq \frac{1}{\Omega_c}\sum_{f\in\mathcal{F}_c} \underline{\psi}_f \cdot \underline{S}_f = \left(\mathrm{div}\left(\underline{\psi}\right)\right)_c, \tag{5}$$

where $\mathcal{F}_c$ is the ensemble of all the planar polygonal faces of the cell c, and $\underline{S}_f$ is the outward surface vector. The discrete cell gradient operator of a field ψ is also defined as the divergence of the tensor $\psi\underline{\underline{I}}$:

$$\underline{\mathrm{Grad}}_c\left(\psi_f\right) \coloneqq \frac{1}{\Omega_c}\sum_{f\in\mathcal{F}_c} \psi_f \underline{S}_f = \left(\underline{\mathrm{div}}\left(\psi\underline{\underline{I}}\right)\right)_c. \tag{6}$$

Finally, the discrete Laplacian operator of a given scalar ψ with coefficient of diffusion K uses the two points flux approximation (TPFA) (see References 53 and 54 for more details) and is defined as:

$$\mathrm{Lap}_c\left(K,\ \psi\right) \coloneqq \frac{1}{\Omega_c}\sum_{f\in\mathcal{F}_c} K\underline{\nabla}_f\psi \cdot \underline{S}_f, \qquad \underline{\nabla}_f\psi = \frac{\psi_{\tilde{c}} - \psi_c}{d_{c\tilde{c}}}. \tag{7}$$

Remark 1. The mass balance is selected to be performed between time steps n and $n+1$. Therefore, since they are linked by the equation of state, scalar mass fractions Y, temperature T and density ρ are stored in the same space and time locations. The mass balance implies that the mass fluxes denoted by $\underline{q}_f \cdot \underline{S}_f$ are stored in the time interval $[n, n+1]$ and on the mesh faces. Note that the time interval $[n, n+1]$ is the dual space of time $n+\frac{1}{2}$. Therefore, the momentum equation is solved between times $n-\frac{1}{2}$ and $n+\frac{1}{2}$ when $\theta = 1/2$. Figure 2 shows the time locations of the different scheme variables. When $\theta = 1/2$, the velocity location is at the center of the time interval $[n, n+1]$, whereas other fields are evaluated at times n and $n+1$, respectively.

2.4 | Time scheme

The equations to be solved are nonlinear. Here, an iterative process is proposed with inner-iterations denoted by the superscript k, starting at 1. It is based on an approach that combines prediction and correction steps, which is often used in incompressible schemes. Moreover, one has to distinguish the thermodynamic pressure, located with the other thermodynamic variables (denoted as p^n for the time t^n), and the mechanical pressure which applies a force on the momentum during the time interval $[n-1+\theta, n+\theta]$ (denoted by $p|_{n-1+\theta}^{n+\theta}$). Their relation is given later in Equation (14).

10970363, 2022, 12, Downloaded from https://onlinelibrary.wiley.com/doi/10.1002/fld.5116 by Jozef Stefan Institute, Wiley Online Library on [07/04/2025]. See the Terms and Conditions (https://onlinelibrary.wiley.com/terms-and-conditions) on Wiley Online Library for rules of use; OA articles are governed by the applicable Creative Commons License

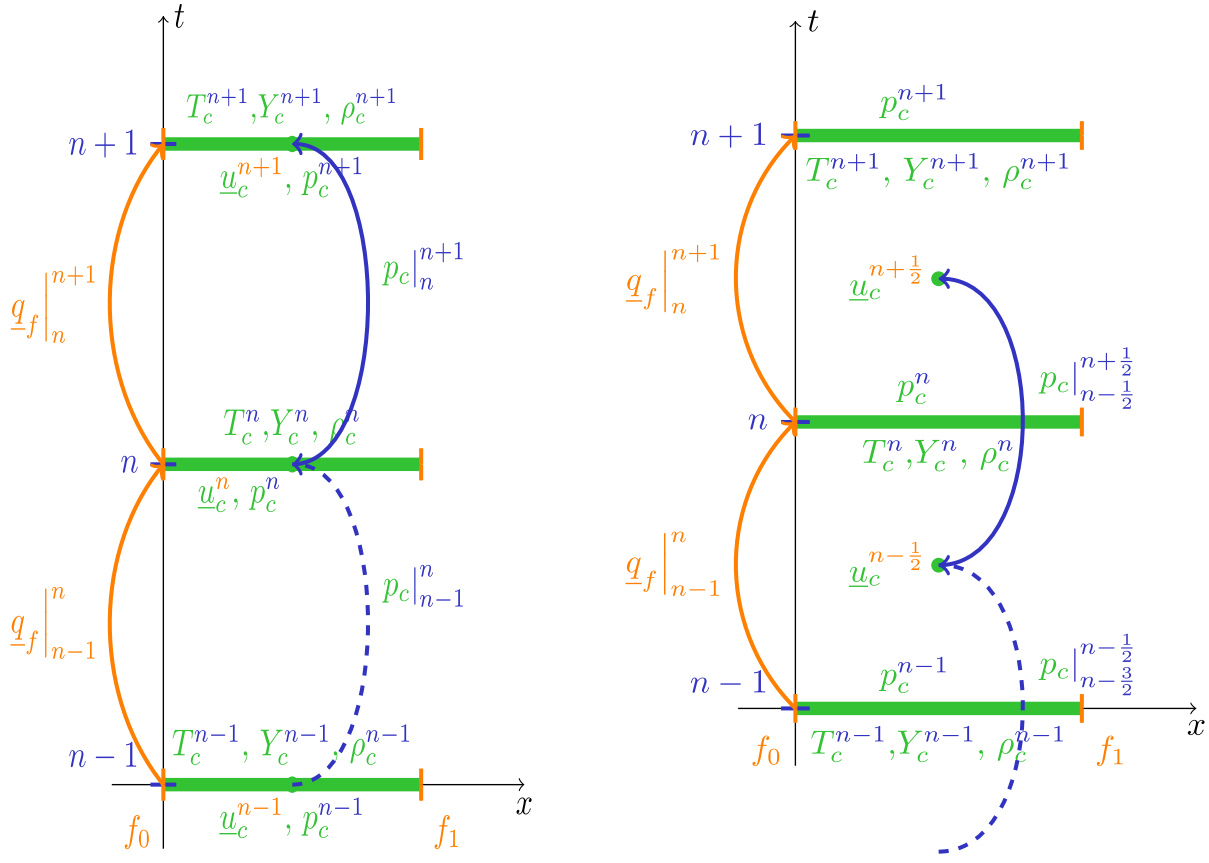

(A) $\theta = 1$ (implicit Euler). (B) $\theta = 1/2$ (Crank Nicolson).

FIGURE 2 Time variables localization for the two θ values [Colour figure can be viewed at wileyonlinelibrary.com]

Three major constraints are considered while designing the proposed scheme.

1. At each step, the instantaneous density must be in coherence with the convective mass flux;
2. To maintain the scheme conservation property, when adding the prediction and correction equations (Equations 10 and 11), unsteady terms of the predicted velocity $\underline{\tilde{u}}^k$ should disappear;
3. The densities of the prediction and correction step are centered at the time step n when $\theta = 1/2$.

For a sake of clarity, the time step Δt is supposed constant from now on. The reader may find the scheme equations for a variable time step in Appendix C.

Time integration

for $n \in [0, N-1]$

- *Initialisation*: for $k = 1$, the cell c initial values are

$$\rho_c^{n,0} = \rho_c^{n-1}, \quad \rho_c^{n+1,0} = \rho_c^n, \quad \underline{q}_f\Big|_n^{n+1,0} \cdot \underline{S}_f = \underline{q}_f\Big|_{n-1}^{n} \cdot \underline{S}_f, \quad p|_{n-1+\theta}^{n+\theta,0} = p^n.$$

As a side note, at any iteration, the mass flux should verify the following mass balance equation:

$$\mathrm{Div}_c\left(\underline{q}_f\Big|_n^{n+1,k}\right) = -\frac{\left(\rho_c^{n+1,k} - \rho_c^{n,k}\right)}{\Delta t}.$$

10970363, 2022, 12, Downloaded from https://onlinelibrary.wiley.com/doi/10.1002/fld.5116 by Jozef Stefan Institute, Wiley Online Library on [07/04/2025]. See the Terms and Conditions (https://onlinelibrary.wiley.com/terms-and-conditions) on Wiley Online Library for rules of use; OA articles are governed by the applicable Creative Commons License

Subiterations for $k \in [1, M-1]$

- *Buoyant scalars step*: scalars $Y_c^{n+1,k}$ and the temperature $T_c^{n+1,k}$ are computed by solving in the interval $[n, n+1]$:

$$\text{(a):}\quad \frac{\rho_c^{n+1,k-1} Y_c^{n+1,k} - \rho_c^{n,k-1} Y_c^{n}}{\Delta t} + \mathrm{Div}_c\left(\left\langle \Theta\left(Y^n,\, Y^{n+1,k}\right)\right\rangle_f \underline{q}_f\Big|_n^{n+1,k-1}\right) = \mathrm{Lap}_c\left(K, \Theta\left(Y^n,\, Y^{n+1,k}\right)\right), \text{for scalars,}$$

$$\text{(b):}\quad c_v\left[\frac{\rho_c^{n+1,k-1} T_c^{n+1,k} - \rho_c^{n,k-1} T_c^{n}}{\Delta t} + \mathrm{Div}_c\left(\left\langle \Theta\left(T^n,\, T^{n+1,k}\right)\right\rangle_f \underline{q}_f\Big|_n^{n+1,k-1}\right)\right] = \mu(S_c^2)^{n+\theta,k-1} + \Gamma_c^{u^2/2}\Big|_n^{n+1,k-1}$$
$$+ \mathrm{Lap}_c\left(\lambda, \Theta\left(T^n,\, T^{n+1,k}\right)\right) - \mathrm{Div}_c\left(\left\langle \Theta\left(p^n,\, p^{n+1,k-1}\right)\underline{u}^{n+\theta,k-1}\right\rangle_f\right) + \underline{u}_c^{n+\theta,k-1}\cdot \underline{\nabla}_c p|_{n-1+\theta}^{n+\theta,k-1}, \text{for temperature.} \tag{8}$$

Note that the term $p\mathrm{div}\,(\underline{u})$, implemented as $\mathrm{div}\,(p\underline{u}) - \underline{u}\cdot\underline{\nabla}(p)$, is calculated using an upwind scheme. Different spatial discretizations can be used for the convection equation term (see Reference 40 for more details). Further, for the first subiteration, $\rho^{n,k-1}$ is ρ^{n-1} and $\rho^{n+1,k-1}$ is ρ^n; thus, the density variation $(\rho^n - \rho^{n-1})$ is balanced by the mass flux $\underline{q}_f\Big|_{n-1}^{n}$ term. $\Gamma_c^{u^2/2}\Big|_n^{n+1,k-1}$ is a corrective source term derived from the discrete kinetic energy equation based on Reference 26 and is derived here for the present sub-iterative scheme:

$$\Gamma_c^{u^2/2}\Big|_n^{n+1,k-1} = \left[1 - \frac{\Theta\left(\rho_c^n,\, \rho_c^{n+1,k-2}\right)}{\Theta\left(\rho_c^n,\, \rho_c^{n+1,k-1}\right)}\right]\left[\Theta\left(\rho_c^{n-1},\, \rho_c^n\right)\frac{|\underline{u}_c^{n-1+\theta}|^2}{2\Delta t} - \mathrm{Div}_c\left(\frac{\left|\left\langle \Theta\left(\underline{u}^{n-1+\theta},\, \tilde{\underline{u}}^{k-1}\right)\right\rangle_f\right|^2}{2}\underline{q}_f\Big|_{n-1+\theta}^{n+\theta,k-2}\right)\right]$$
$$- \frac{\Theta\left(\rho_c^n,\, \rho_c^{n+1,k-2}\right)}{\Theta\left(\rho_c^n,\, \rho_c^{n+1,k-1}\right)}\mathrm{Div}_c\left(\frac{\left|\left\langle \Theta\left(\underline{u}^{n-1+\theta},\, \tilde{\underline{u}}^{k-1}\right)\right\rangle_f - \underline{u}_c^{k-1}\right|^2}{2}\underline{q}_f\Big|_{n-1+\theta}^{n+\theta,k-2}\right)$$
$$+ \frac{\Theta\left(\rho_c^n,\, \rho_c^{n+1,k-2}\right)}{\Theta\left(\rho_c^n,\, \rho_c^{n+1,k-1}\right)}\Theta\left(\rho_c^{n-1},\, \rho_c^n\right)\frac{\left[|\underline{u}_c^{k-1} - \underline{u}_c^{n-1+\theta}|^2\right]}{2\Delta t}. \tag{9}$$

All face values $\left\langle \Theta\left(\underline{u}^{n-1+\theta},\, \tilde{\underline{u}}^{k-1}\right)\right\rangle_f$ were obtained using the same convective scheme as that used for the convection term during the prediction equation (Equation 10). This corrective term allows the total energy to be conserved in the given interval, leading to consistent solutions even in the presence of irregularities. The derivation is given in Appendix A.

- An intermediate density is calculated with the equation of state*

$$\tilde{\rho}_c^{\,k} = \varrho\left(p_c^{n+1,k-1}, T_c^{n+1,k}\right) = \frac{p_c^{n+1,k-1}}{R_a T_c^{n+1,k}}, \qquad \text{for ideal gases.}$$

This new density is not balanced by any mass flux. The mass conservation is insured in the correction step.

- *Prediction step*: An intermediate velocity $\tilde{\underline{u}}^k$ is computed by solving the momentum equation in the time interval $[n-1+\theta, n+\theta]$:

$$\frac{\Theta\left(\rho_c^n,\, \rho_c^{n+1,k-1}\right)\tilde{\underline{u}}_c^k - \Theta\left(\rho_c^{n-1},\, \rho_c^{n,k-1}\right)\underline{u}_c^{n-1+\theta}}{\Delta t} + \mathrm{Div}_c\left(\left\langle \Theta\left(\underline{u}^{n-1+\theta},\, \tilde{\underline{u}}^{k}\right)\right\rangle_f \otimes \underline{q}_f\Big|_{n-1+\theta}^{n+\theta,k-1}\right)$$
$$= -\underline{\mathrm{Grad}}_c\left(\left\langle p|_{n-1+\theta}^{n+\theta,k-1}\right\rangle_f\right) + \mathrm{Div}_c\left(\underline{\underline{\tau}}_f^k\right) + \underline{f}_c\Big|_{n-1+\theta}^{n+\theta,k-1}. \tag{10}$$

The mass flux $\underline{q}_f\Big|_{n-1+\theta\ f}^{n+\theta,k-1}$ is defined by $\underline{q}_f\Big|_{n-1+\theta}^{n+\theta,k-1} = \Theta\left(\underline{q}_f\Big|_{n-1}^{n}, \underline{q}_f\Big|_{n}^{n+1,k-1}\right)$. Note that the cell pressure gradient and external volume force are taken at the same time interval; if they are in a partial balance, no parasite velocities

10970363, 2022, 12, Downloaded from https://onlinelibrary.wiley.com/doi/10.1002/fld.5116 by Jozef Stefan Institute, Wiley Online Library on [07/04/2025]. See the Terms and Conditions (https://onlinelibrary.wiley.com/terms-and-conditions) on Wiley Online Library for rules of use; OA articles are governed by the applicable Creative Commons License

are created. Similar to the temperature equation, face terms $\langle . \rangle_f$ related to the material convection can be evaluated through different convective schemes available in code_saturne.[40] The face pressure is computed using a centered interpolation.

- *Correction step*: During this stage, the pressure increment $\phi^k = p\big|_{n-1+\theta}^{n+\theta,k} - p\big|_{n-1+\theta}^{n+\theta,k-1}$ is computed and used to correct the velocity $\underline{u}^{n+\theta,k}$. The following system is solved on $[n, n+1]$:

$$\begin{cases} \dfrac{\Theta\left(\rho_c^n,\, \rho_c^{n+1,k}\right)\underline{u}_c^{n+\theta,k} - \Theta\left(\rho_c^n,\, \rho_c^{n+1,k-1}\right)\underline{\tilde{u}}_c^k}{\Delta t} + \underline{\nabla}_f \phi^k = \delta \underline{f}_c^k, \qquad \text{with } \delta \underline{f}_c^k = \underline{f}_c\big|_{n-1+\theta}^{n+\theta,k} - \underline{f}_c\big|_{n-1+\theta}^{n+\theta,k-1}, \\ \mathrm{Div}_c\left(\underline{q}_f\Big|_n^{n+1,k}\right) + \dfrac{\rho_c^{n+1,k} - \rho_c^n}{\Delta t} = 0, \end{cases} \tag{11}$$

where, by definition:

$$\underline{q}_f\Big|_n^{n+1,k} = \left\langle \Theta\left(\rho^n,\, \rho^{n+1,k}\right)\underline{u}^{n+\theta,k}\right\rangle_f = \left\langle \Theta\left(\rho^n,\, \rho^{n+1,k-1}\right)\underline{\tilde{u}}^k\right\rangle_f - \Delta t\left(\underline{\nabla}_f \phi^k - \delta \underline{f}_c^k\right), \tag{12}$$

which verifies the mass balance with $\dfrac{\rho_c^{n+1,k} - \rho_c^n}{\Delta t}$, and whose field face values are calculated using a centered scheme. Combining the equations in (11) and using the Rhie and Chow[55] filter leads to a Helmholtz equation for the cell thermodynamic pressure $p_c^{n+1,k}$:

$$\begin{aligned} \frac{\rho_c^{n+1,k} - \rho_c^n}{\Delta t} - \theta \mathrm{Lap}_c\left(\Delta t, p^{n+1,k}\right) = &-\mathrm{Div}_c\left(\left\langle \Theta\left(\rho^n,\, \rho^{n+1,k-1}\right)\underline{\tilde{u}}^k + \Delta t\left(\underline{\nabla} p\big|_{n-1+\theta}^{n+\theta,k-1} + \delta \underline{f}^k\right)\right\rangle_f\right) \\ &+ (1-\theta)\mathrm{Lap}_c\left(\Delta t, p\big|_{n-2+\theta}^{n-1+\theta}\right). \end{aligned} \tag{13}$$

The pressure $p_c^{n+1,k}$ is linked to ϕ_c^k through:

$$\phi_c^k = \Theta\left(p_c\big|_{n-2+\theta}^{n-1+\theta},\, p_c^{n+1,k}\right) - p_c\big|_{n-1+\theta}^{n+\theta,k-1}. \tag{14}$$

The density $\rho_c^{n+1,k}$ reads:

$$\begin{aligned} \rho_c^{n+1,k} &= \tilde{\rho}_c^k + \left(p_c^{n+1,k} - p_c^{n+1,k-1}\right)\left(\frac{\partial \varrho}{\partial p}\Big|_T\left(T_c^{n+1,k}, p_c^{n+1,k-1}\right)\right), \\ &= \frac{p_c^{n+1,k}}{R_a T_c^{n+1,k}}, \qquad \text{for ideal gases.} \end{aligned} \tag{15}$$

Note that the update of density performed in the first line of (15) makes the scheme conservative in space and time for mass, which is an important property for nonregular solutions. From a generic point of view, the density $\rho^{n+1,k}$ in equation (15) might not satisfy the equation of state (contrary to what was done in step 6 of Reference 30). In the case of an ideal gas, the first line of (15) reduces to the second line of (15). The sub-iterative process for the time step ends when the error $\epsilon^k = \sqrt{\sum_{c=1}^{N_{cell}} \Omega_c \left|\underline{u}_c^{n+\theta,k} - \underline{u}_c^{n+\theta,k-1}\right|^2}$ is below a fixed value ϵ_0. The scheme main steps, showing the primary variables solved and their related equations are summarized in Algorithm 1.

2.5 | Properties of the scheme

In this section, we present the different Courant and Fourier like sufficient conditions to ensure the temperature, pressure and density positivity. An upwind convective scheme was used to evaluate the face field values. The proofs of the CPC scheme Properties 1–3 summarized in this section are given in Appendix B.

10970363, 2022, 12, Downloaded from https://onlinelibrary.wiley.com/doi/10.1002/fld.5116 by Jozef Stefan Institute, Wiley Online Library on [07/04/2025]. See the Terms and Conditions (https://onlinelibrary.wiley.com/terms-and-conditions) on Wiley Online Library for rules of use; OA articles are governed by the applicable Creative Commons License

Algorithm 1. Time scheme main steps

First time step initialization
Time loop
for `n = 0, N-1` **do**
  Initialization of variables at the first sub-iteration $k = 1$
  for `k = 0, M-1` **do**
    Compute scalars and temperature $Y_c^{n+1,k}, T_c^{n+1,k}$, Eq (8)
    Update of the density $\tilde{\rho_c}$ with $T_c^{n+1,k}$
    Compute the predicted velocity $\underline{u_c}^k$, Eq (10)
    Correction step: compute $\phi_c^k \rightarrow p_c|_{n-1+\theta}^{n+\theta}$, Eq (13)
    Correct the thermodynamic pressure $p_c^{n+1,k}$, Eq (14)
    Correct the density $\rho_c^{n+1,k}$, Eq (15)
    Correct the velocity $\underline{u}_c^{n+\theta,k}$, Eq (12)
    if $\epsilon^k \leq \epsilon_0$ **then**
      Break the for loop
    else
      Compute the kinetic energy source term $\Gamma_c^{u^2/2}\Big|_n^{n+1}$, Eq (9)
    end if
  end for
end for

Property 1 (Positivity of the temperature). Assume an upwind convective scheme and initial conditions for all cells; ρ_c^0, T_c^0 and p_c^0 are positive; and an ideal gas with $\gamma > 1$. Assume that the corrective source term $\Gamma_c^{u^2/2}$ is positive. Then, the temperature $T_c^{n+1,k}$ will remain positive for all cells, provided that the time step Δt complies with the CFL (Equations 16 and 17) conditions and the Fourier Equation (18) condition.

$$CFL_{T_1}^+ < 1 \text{ where } CFL_{T_1}^+ \coloneqq (1-\theta)\frac{\Delta t}{M_c^n}\sum_{f\in\mathcal{F}_c}\dot{M}_f^+\Big|_n^{n+1,k-1}. \tag{16}$$

$$CFL_{T_2}^+ < 1 \text{ where } CFL_{T_2}^+ \coloneqq \frac{\Delta t}{M_c^n}\sum_{f\in\mathcal{F}_c}\left[\theta(\gamma-1)\frac{T_c^{n+1,k-1}}{T_c^n}+(1-\theta)\gamma\right]\dot{M}_f^+\Big|_n^{n+1,k-1} - \frac{\Delta t(\gamma-1)\underline{u}_c^{n+\theta,k-1}\cdot\underline{\nabla}_c p|_{n-1+\theta}^{n+\theta,k-1}}{p_c^n}. \tag{17}$$

$$Fo_T^+ < 1 \text{ where } Fo_T^+ \coloneqq \frac{\lambda_c(1-\theta)\Delta t}{c_v M_c^n}\sum_{f\in\mathcal{F}_c}|\underline{S}_f|. \tag{18}$$

Property 2 (Positivity of the pressure). Assume an upwind scheme and initial conditions for all cells, ρ_c^0 T_c^0 and p_c^0 and an ideal gas with $\gamma > 1$. Then, the pressure $p_c^{n+1,k}$ will remain positive for all cells provided that the time step Δt complies with the CFL condition (19).

$$CFL_p^+ < 1 \text{ where } CFL_p^+ \coloneqq \frac{\Delta t}{M_c^n}\sum_{f\in\mathcal{F}_c}a_f^\phi. \tag{19}$$

where

$$a_f^\phi = \left\langle \Theta\left(\rho^n,\, \rho^{n+1,k-1}\right)\underline{\tilde{u}}^k + \Delta t\underline{\nabla} p|_{n-1+\theta}^{n+\theta,k-1}\right\rangle_f \cdot \underline{S}_f - (1-\theta)\Delta t\underline{\nabla}_f p|_{n-2+\theta}^{n-1+\theta}\cdot\underline{S}_f$$

Property 3 (Positivity of density). Assume an upwind scheme, initial conditions for all cells; ρ_c^0, T_c^0 and p_c^0 are positive; and an ideal gas with $\gamma > 1$, then the density $\rho_c^{n+1,k}$ will remain positive if the conditions (16), (17), (18), and (19) are respected.

Property 4 (Scheme low Mach number limit). By defining the sound speed $\frac{1}{c^2} = \frac{\partial\varrho}{\partial p}\Big|_S \approx \frac{\partial\varrho}{\partial p}\Big|_T$, the Helmholtz Equation (13) can be rewritten as

10970363, 2022, 12, Downloaded from https://onlinelibrary.wiley.com/doi/10.1002/fld.5116 by Jozef Stefan Institute, Wiley Online Library on [07/04/2025]. See the Terms and Conditions (https://onlinelibrary.wiley.com/terms-and-conditions) on Wiley Online Library for rules of use; OA articles are governed by the applicable Creative Commons License

$$\frac{p_c^{n+1,k} - p_c^{n+1,k-1}}{c^2\ \Delta t} - \theta \mathrm{Lap}_c\left(\Delta t, p^{n+1,k}\right) = -\frac{\tilde{\rho}_c^k - \rho_c^n}{\Delta t} - \mathrm{Div}_c\left(\left\langle \Theta\left(\rho^n,\ \rho^{n+1,k-1}\right)\underline{\tilde{u}}^k + \Delta t\left(\underline{\nabla} p|_{n-1+\theta}^{n+\theta,k-1} + \delta \underline{f}^k\right)\right\rangle_f\right) + (1-\theta)\mathrm{Lap}_c\left(\Delta t, p|_{n-2+\theta}^{n-1+\theta}\right). \tag{20}$$

By introducing the Mach number $Ma = \frac{u_{ref}}{c}$ with u_{ref} as a characteristic velocity, the order of magnitude of the first term on the left-hand side is $Ma^2 \frac{\delta P}{\rho_{ref} u_{ref}^2} \frac{\rho_{ref}}{\Delta t}$. In the limit of the zero-Mach number, this term is negligible compared with the first term on the right-hand side. The Helmholtz equation becomes a Poisson equation, similar to the one used for incompressible flow with variable density.[40]

3 | SCHEME VERIFICATION AND VALIDATION

The CPC scheme is verified on analytical test cases and validated on reference numerical and experimental cases. Note that for all simulations, a constant time step was used and the density follows the ideal gas law.

3.1 | Pressure cooker like system

This verification case is designed to test the time scheme ability to take into account pressure variations while conserving the global mass of the system, composed of a single computational cell of $[1 \times 1 \times 1]$ m^3. Two faces are heated while others present adiabatic boundary conditions as displayed on Figure 3. Two different cases are considered where the boundary conditions change. First, a Neumann boundary condition on the heated walls is considered and then a Dirichlet boundary condition is tested. The initial system temperature and density are set as $T_0 = 300$ K and $\rho_0 = 1.177$ kg m^{-3} for both cases. For a field ψ, the numerical ψ_c and analytical ψ_{ex} results are compared through the mean square relative error $L_2^{\mathrm{err}}(\psi)$ over the cell c of volume Ω_c:

$$L_2^{\mathrm{err}}(\psi) := \sqrt{\frac{\frac{1}{\Omega_{tot}}\sum_c (\psi_c - \psi_{ex})^2 \Omega_c}{\frac{1}{\Omega_{tot}}\sum_c \psi_0^2 \Omega_c}}. \tag{21}$$

The system analytical temperature expressions for the Neumann (N) and Dirichlet (D) cases are:

$$T_{\mathrm{N}}(t) = T_0\left(1 + \frac{t}{\tau_1}\right), \qquad T_{\mathrm{D}}(t) = \left(T_0 - T_p\right)\ e^{-\frac{t}{\tau_2}} + T_p, \tag{22}$$

where $\tau_1 = \frac{\Omega_{tot}\ \rho_0\ c_v\ T_0}{S\ Q_i}$, $\tau_2 = \frac{\Omega_{tot}\ \rho_0\ c_v}{S\ h}$ and $Q_i = 5$ W m^{-2}. Here, Ω_{tot} is the total cell volume, c_v is the heat capacity, and S is the total heated wall surface. $T_p = 313$ K denotes the wall temperature. The interior air heat transfer coefficient $h = 30$ W m^{-2} K^{-1} remains constant and the time step is set as $\Delta t = 1\ s$, with a single inner-iteration.

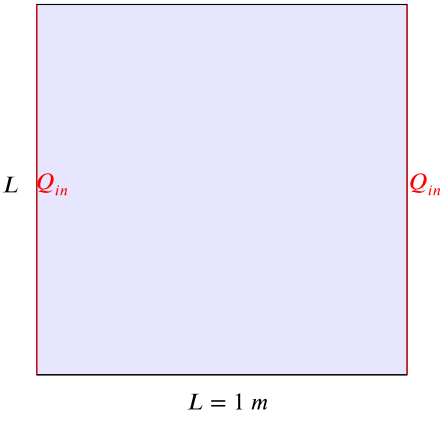

FIGURE 3 Sketch of the system [Colour figure can be viewed at wileyonlinelibrary.com]

10970363, 2022, 12, Downloaded from https://onlinelibrary.wiley.com/doi/10.1002/fld.5116 by Jozef Stefan Institute, Wiley Online Library on [07/04/2025]. See the Terms and Conditions (https://onlinelibrary.wiley.com/terms-and-conditions) on Wiley Online Library for rules of use; OA articles are governed by the applicable Creative Commons License

The CPC scheme results are compared with the analytical and IPC scheme results. Figure 4 shows the L_2 error norm for the different fields over time; the presented algorithm takes into account the pressure variation while the cell is heated (Figure 4, black lines) whereas the IPC scheme, which uses the Poisson equation in the correction step, leads to more important and increasing errors (red lines). Moreover, the errors are below the solver precision for all variables, fixed as 10^{-8}. Note that the increasing behavior of all errors can be explained as an accumulation of truncation errors. Figure 5 shows the pressure L_2 error at $t = 0.8\tau_2$ s for the Dirichlet boundary condition study. It is verified that the first and second order time convergence rate are obtained when $\theta = 1$ and $1/2$, respectively.

3.2 | 1D convection verification case

This test case is designed to verify the scheme conservation of the mass and momentum over time as well as its time convergence order while transporting a scalar for a flow of constant velocity. The one-dimensional domain has a length L of 40 m and a 40 cells Cartesian mesh is used. The constant velocity flow is considered laminar and viscous terms are disabled. The temperature inlet boundary condition is varied over time as follows:

$$T_{in} = 473 \text{ K} \quad \text{if } t \in [10, 20[, \quad T_{in} = 300 \text{ K} \quad \text{otherwise.}$$

The inlet velocity is set as $U_0 = 1$ m s^{-1} and the initial density as $\rho_0 = 1.177$ kg m^{-3}. The outlet pressure is set to the reference value p_0 and all other walls are considered as symmetries. Mass and momentum balances are then performed

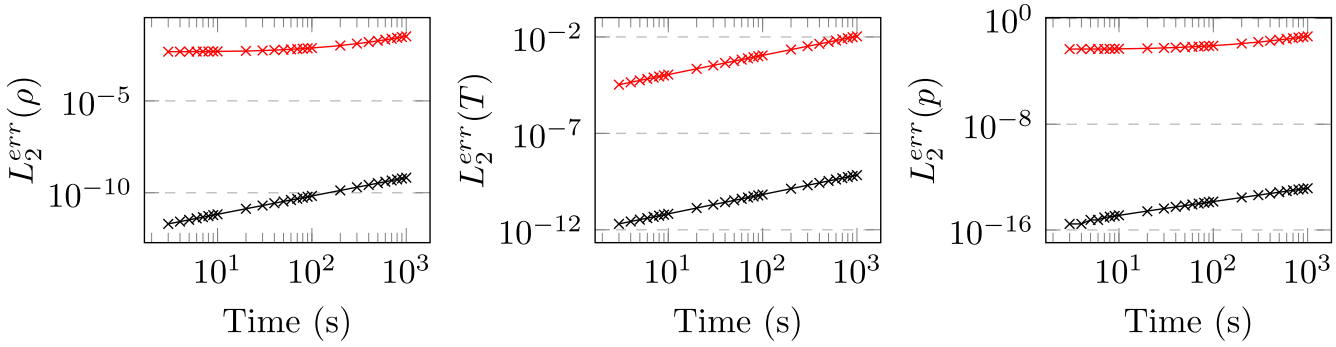

FIGURE 4 L_2 error norm of the density, temperature, and pressure for the Neumann boundary condition case. (____) IPC[46] code_saturne scheme. (–) presented scheme [Colour figure can be viewed at wileyonlinelibrary.com]

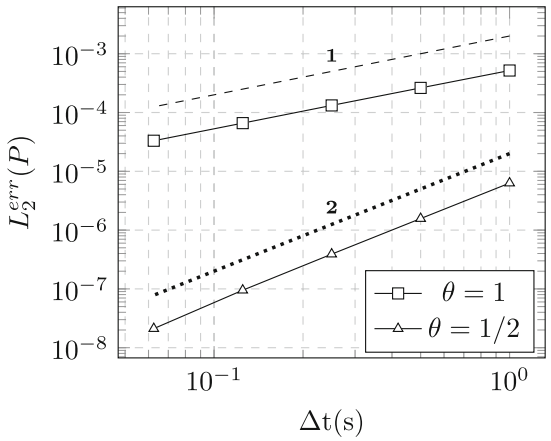

FIGURE 5 Dirichlet boundary condition case. L_2 error for the pressure at $t = 0.8\tau_2$ for a first-order implicit Euler ($\theta = 1$) and Crank Nicolson ($\theta = 1/2$) time scheme

10970363, 2022, 12, Downloaded from https://onlinelibrary.wiley.com/doi/10.1002/fld.5116 by Jozef Stefan Institute, Wiley Online Library on [07/04/2025]. See the Terms and Conditions (https://onlinelibrary.wiley.com/terms-and-conditions) on Wiley Online Library for rules of use; OA articles are governed by the applicable Creative Commons License

over the entire system and normalized by their initial values for each time step as follows:

$$I_\rho = \frac{\int_\Omega \rho^n \mathrm{d}\Omega + \int_{t=0}^{t^n} \int_{\partial\Omega} \rho u \mathrm{d}S_x \mathrm{d}t}{\int_\Omega \rho_0 \mathrm{d}\Omega}, \qquad I_q = \frac{\int_\Omega (\rho u)^{n-\theta} \mathrm{d}\Omega + \int_{t=0}^{t^{n-\theta}} \int_{\partial\Omega} (\rho u u + p)\, \mathrm{d}S_x \mathrm{d}t}{\int_\Omega \rho_0 u_0 \mathrm{d}\Omega}. \tag{23}$$

The conservation of both quantities is tested for $\theta = 1$ and $\theta = 1/2$. For each time step, set as $\Delta t = 0.3$ s, 5 inner-iterations are performed. The results of this study (Figures 6 and 7) show that the variation of mass and momentum relative to their initial values are below 10^{-7} for both simulations, validating their conservation.

A second study was conducted to verify the CPC scheme time convergence rate while transporting a passive scalar. The latter is initialized following two different profiles:

$$Y(x,0) = Y_0 \ \exp(-(x/L-5)^2) \qquad \text{and} \qquad Y(x,0) = Y_0 \ \tanh(x/L-5),$$

where $Y_0 = 1$ denotes the initial constant. The source and diffusive terms being disabled, an exact solution for the scalar can be derived from its transport equation and compared to the numerical solution through its L_2 error norm:

$$\frac{\partial Y}{\partial t} + U_0 \frac{\partial Y}{\partial x} = 0 \rightarrow Y(x,t) = Y(x - U_0 t, 0), \tag{24}$$

where U_0 is the inlet velocity set as 0.1 m s^{-1}.

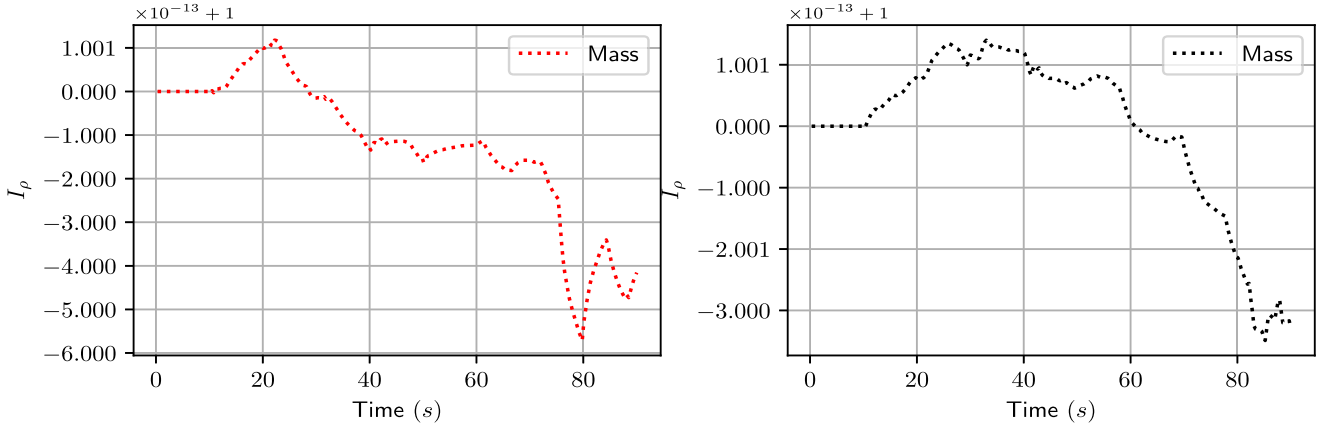

FIGURE 6 Mass conservation for the (left) Euler implicit scheme ($\theta = 1$) and the (right) Crank Nicolson scheme ($\theta = 1/2$) [Colour figure can be viewed at wileyonlinelibrary.com]

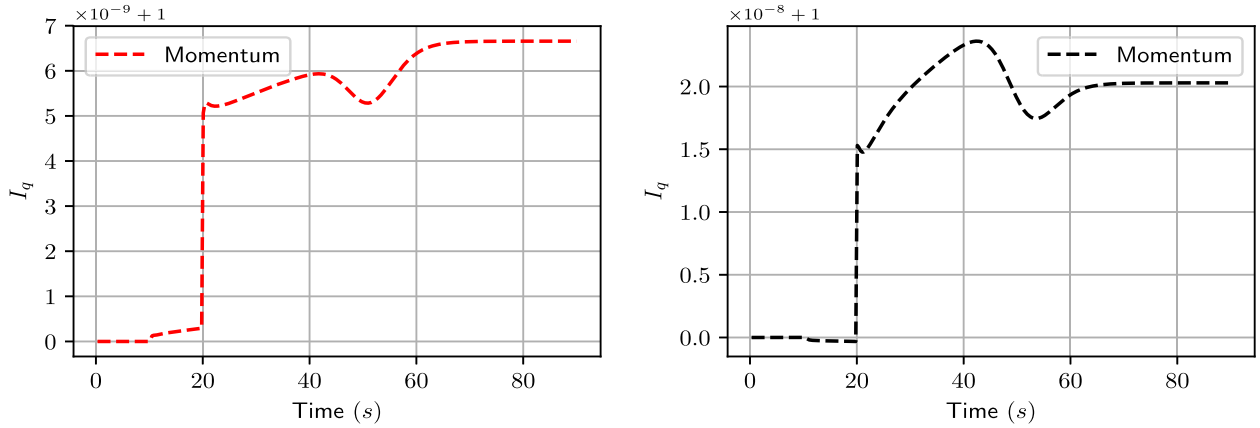

FIGURE 7 Momentum conservation for the (left) Euler implicit scheme ($\theta = 1$) and the (right) Crank Nicolson scheme ($\theta = 1/2$) [Colour figure can be viewed at wileyonlinelibrary.com]

10970363, 2022, 12, Downloaded from https://onlinelibrary.wiley.com/doi/10.1002/fld.5116 by Jozef Stefan Institute, Wiley Online Library on [07/04/2025]. See the Terms and Conditions (https://onlinelibrary.wiley.com/terms-and-conditions) on Wiley Online Library for rules of use; OA articles are governed by the applicable Creative Commons License

At the fixed time $t = 45$ s, the scalar L_2 error norm was studied following the spatial grid refinement at the constant Courant number $CFL = \dfrac{\Delta t U_0}{\Delta x} = 0.05$ and for different convective schemes (see Reference 40 for a detailed description of code_saturne convective schemes). Four inner-iterations are performed for each time step. Results (Figure 8) show that the scheme converges to the first order when using the upwind scheme for both test cases. When using the centered and second order linear upwind (SOLU)[56] convective schemes, a similar behavior was observed related to the second order. This 1D convective setup provided results that were able to ensure the conservation of mass and momentum by the CPC scheme. Its convergence rate while transporting a scalar was also verified through two scalar profiles and different spatial convective schemes.

3.3 | Shock tube

Two one-dimensional Riemann problems are considered to verify the scheme accuracy for flows with shock and rarefaction waves. First, a double symmetric rarefaction wave expansion is studied and then a more irregular configuration (Sod shock tube[57]). The simulations are carried out on grids with $2^m \times 800$ cells, $0 \leq m \leq 5$. The initial conditions are given in Table 1. The computational domain is a tube of length $L = 400$ m extending from $x = -L/2$ to $x = L/2$, the interface being located at $x = 0$. Symmetry conditions are imposed on all boundary faces of the computational domain except at the two end faces of the tube, which are set to be outlets. For each case, the fields L_1 error norm (related to the Riemann problem exact solution ψ_e, Equation (25)) time convergence rate $\alpha(L_1^{err}(\psi))$ is studied for both θ values and for two fluid-velocity based CFL numbers ($CFL = 0.04$ and $CFL = 1.00$). They are calculated using Equation (25) and the data from the two most refined meshes for each configuration. Independently of the time step, results are achieved with 3 inner-iterations.

$$L_1^{err}(\psi) = \frac{\sum_{c=1}^{N_c} |\Omega_c| \; |\psi_e(x_c) - \psi_c|}{\sum_{c=1}^{N_c} |\Omega_c| \; |\psi_e(x_c)|}, \qquad \alpha(L_1^{err}(\psi)) = \frac{\left| L_1^{err}(\psi)\Big|_{m=5} - L_1^{err}(\psi)\Big|_{m=4} \right|}{12800}. \tag{25}$$

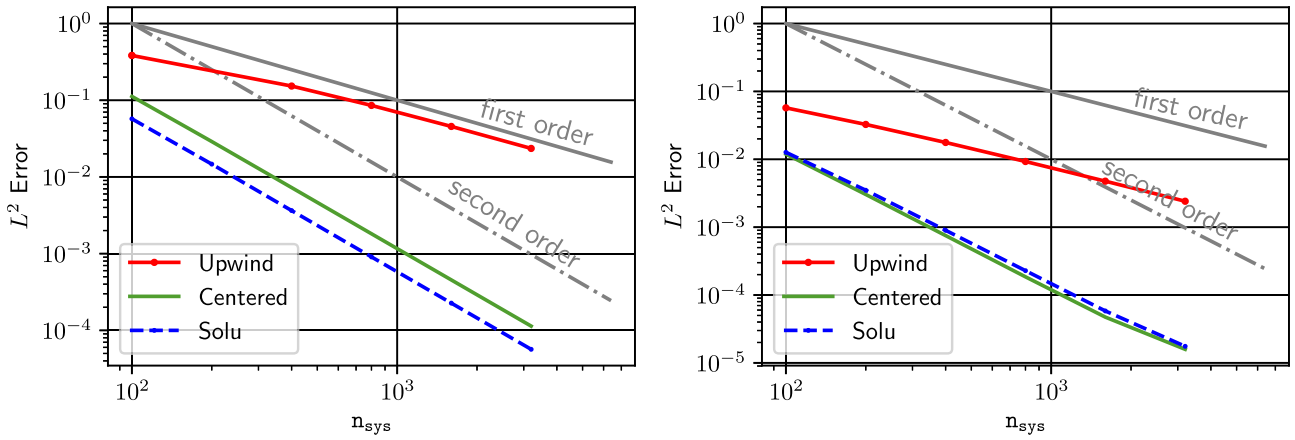

FIGURE 8 Scalar L_2 error norm following the grid refinement for three different convective schemes for the (left) Gaussian scalar initialization and (right) tanh scalar initialization [Colour figure can be viewed at wileyonlinelibrary.com]

TABLE 1 Initial states for the two one-dimensional Riemann problems used

Test	ρ_L(kg m^{-3})	u_L(m s^{-1})	p_L(Pa)	ρ_R(kg m^{-3})	u_R(m s^{-1})	p_R(Pa)
DSE	1	−100	100,000	1	100	100,000
SOD	1	0	100,000	0.125	0	10,000

10970363, 2022, 12, Downloaded from https://onlinelibrary.wiley.com/doi/10.1002/fld.5116 by Jozef Stefan Institute, Wiley Online Library on [07/04/2025]. See the Terms and Conditions (https://onlinelibrary.wiley.com/terms-and-conditions) on Wiley Online Library for rules of use; OA articles are governed by the applicable Creative Commons License

3.3.1 | Double symmetric expansion case

For all fields, the simulation results convergence rates are close to 0.8 for the $CFL = 0.04$ simulations (Figure 9, and Table 2). A slight improvement can be observed when $\theta = 1/2$. For the cases with $CFL = 1.00$, the theta value seems to have a more important impact on the numerical results: again, the convergence rates are higher (close to 1) when using the time staggered scheme. Figure 10 shows the simulation fields at $t = 0.3$s, for a mesh composed of 3200 cells. The different fields are in agreement with the analytical solution. This confirms the scheme accuracy related to regular solutions.

3.3.2 | Sod case

This test case is used to show the importance of adding the source term $\Gamma^{u^2/2}$ to the internal energy equation. Based on the numerical results (Figure 11), one can notice that without the source term, even if the pressure, velocity and density values are close to the exact solution, the correct temperature plateau value is incorrect (Figure 11, blue lines). When using the source term (Figure 11, red lines), the temperature plateau value is well reached by the simulation, leading to consistent numerical results.

Table 3 shows the fields L_1 error convergence rate that are represented in Figure 12 and 13. For irregular solutions, it is known that even second order schemes used for compressible flows do not exhibit second order accuracy. The convergence rates are around 0.5 for the density and temperature and around 1.0 for the pressure and velocity. They can be actually comparable and in agreement with the convergence rates available in the literature for compressible flow solvers.[3,26,47] Similarly to the previous case, when using the staggered scheme ($\theta = 1/2$), the overall L_1 error for all fields is less important than the one obtained with $\theta = 1$.

Finally, Figure 14 shows that for the SOD configuration, the *CFL* like conditions presented in Section 2.5 are respected and below the speed-based *CFL* number for both calculations.

3.4 | Heated cavity: 2-D natural convection

This natural convection validation case presented in Reference 58 and studied in References 59-62 focuses on the heat transfer in a steady flow driven by buoyancy effects at $Ra = 10^6$. The corresponding 2-D system of characteristic length

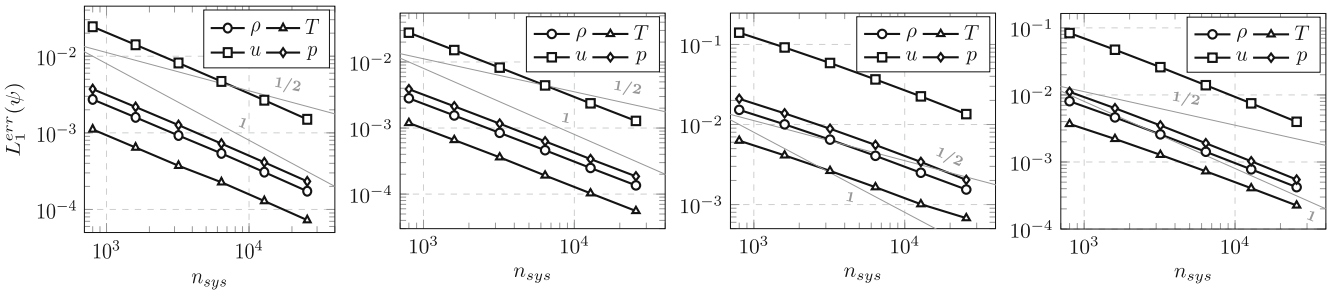

(A) $CFL = 0.04, \theta = 1.$ (B) $CFL = 0.04, \theta = 1/2.$ (C) $CFL = 1.0, \theta = 1.$ (D) $CFL = 1.0, \theta = 1/2.$

FIGURE 9 L_1 error convergence for the DSE case using an upwind convective scheme for two values of *CFL* and θ

TABLE 2 L_1 convergence rates for the DSE case

CFL	θ	ρ rate	$\underline{u}$ rate	p rate	T rate
0.04	1.00	0.83	0.83	0.83	0.83
0.04	0.50	0.88	0.88	0.87	0.89
1.00	1.00	0.49	0.73	0.74	0.58
1.00	0.50	0.88	0.91	0.91	0.85

10970363, 2022, 12, Downloaded from https://onlinelibrary.wiley.com/doi/10.1002/fld.5116 by Jozef Stefan Institute, Wiley Online Library on [07/04/2025]. See the Terms and Conditions (https://onlinelibrary.wiley.com/terms-and-conditions) on Wiley Online Library for rules of use; OA articles are governed by the applicable Creative Commons License

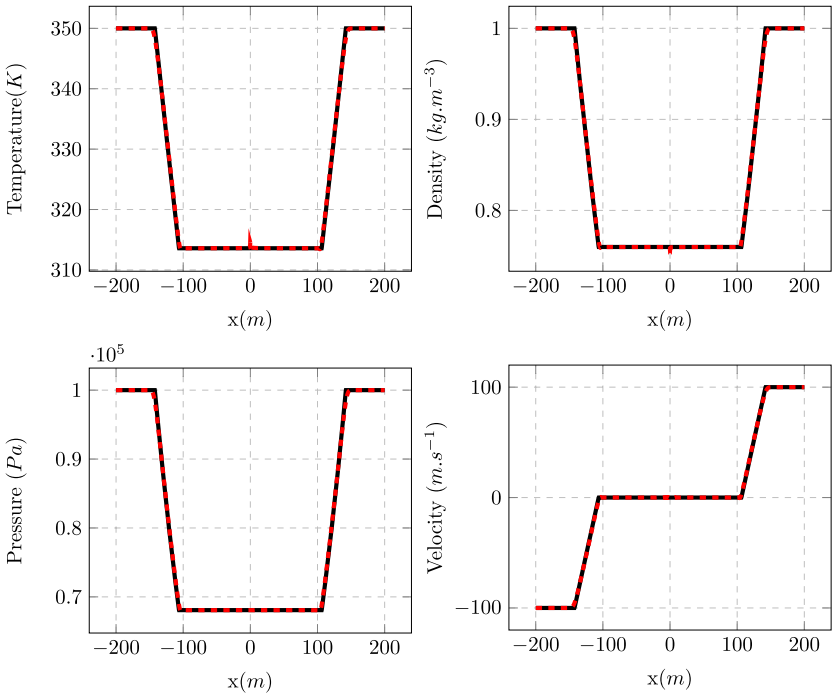

FIGURE 10 Double symmetric expansion wave results at $t = 0.3$ s using a 3200 mesh and for $\theta = 1$ (–) exact solution (.....) simulation [Colour figure can be viewed at wileyonlinelibrary.com]

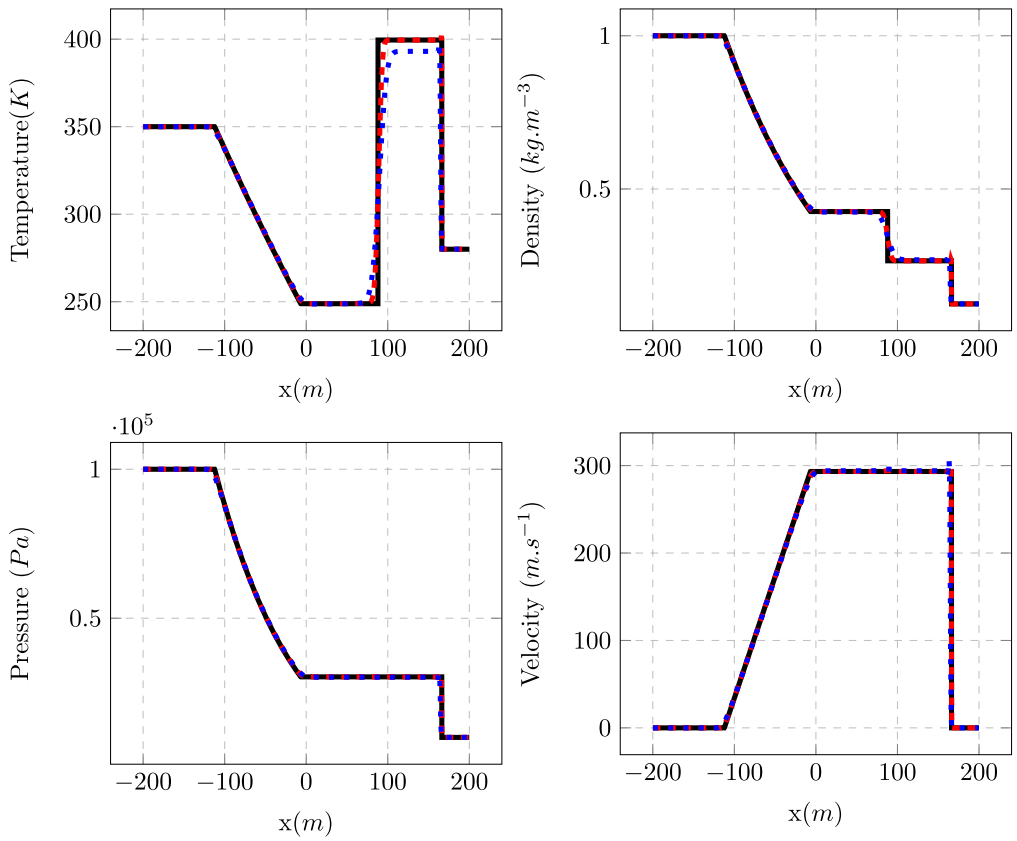

FIGURE 11 SOD case results at $t = 0.3$ s for $\theta = 1$ using a 3200 cells mesh (–) exact solution (.....) simulation using the source term $\Gamma^{u^2/2}$ (.....) simulation without the source term $\Gamma^{u^2/2}$[Colour figure can be viewed at wileyonlinelibrary.com]

10970363, 2022, 12, Downloaded from https://onlinelibrary.wiley.com/doi/10.1002/fld.5116 by Jozef Stefan Institute, Wiley Online Library on [07/04/2025]. See the Terms and Conditions (https://onlinelibrary.wiley.com/terms-and-conditions) on Wiley Online Library for rules of use; OA articles are governed by the applicable Creative Commons License

TABLE 3 Convergence rate for the SOD case

CFL	θ	Convective scheme	ρ rate	$\underline{u}$ rate	p rate	T rate
0.04	1	Upwind	0.60	0.88	0.86	0.54
0.04	0.5	Upwind	0.59	0.86	0.85	0.53
1.00	1	Upwind	0.65	0.89	0.82	0.54
1.00	0.5	Upwind	0.59	0.90	0.85	0.53
0.04	1	Centered	0.61	0.96	0.92	0.53
0.04	0.5	Centered	0.60	0.95	0.95	0.54
1.00	1	Centered	0.64	0.89	0.82	0.56
1.00	0.5	Centered	0.56	0.90	0.89	0.51

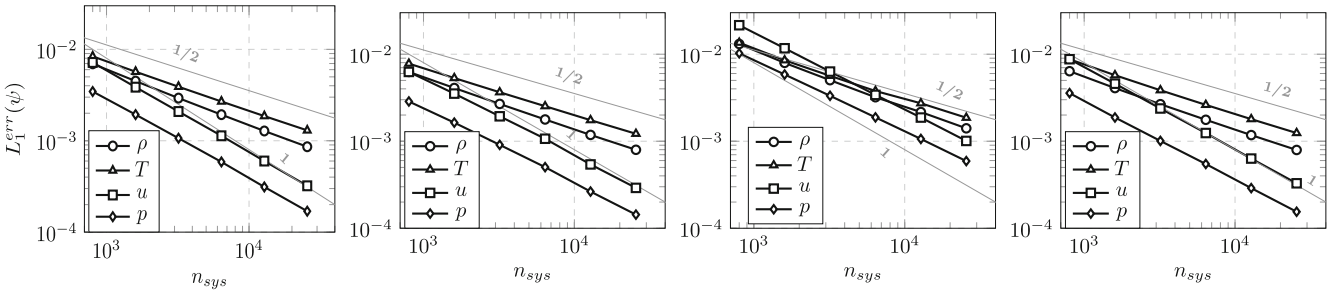

(A) $CFL = 0.04, \theta = 1.$ (B) $CFL = 0.04, \theta = 1/2.$ (C) $CFL = 1.0, \theta = 1.$ (D) $CFL = 1.0, \theta = 1/2.$

FIGURE 12 L_1 error convergence for the SOD case using an upwind convective scheme for two values of *CFL* and θ

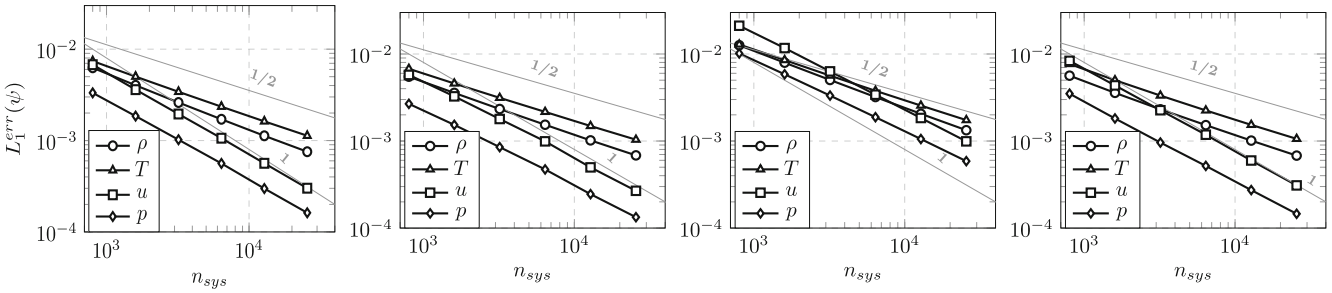

(A) $CFL = 0.04, \theta = 1.$ (B) $CFL = 0.04, \theta = 1/2.$ (C) $CFL = 1.0, \theta = 1.$ (D) $CFL = 1.0, \theta = 1/2.$

FIGURE 13 L_1 error convergence for the SOD case using a centered convective scheme for two values of *CFL* and θ

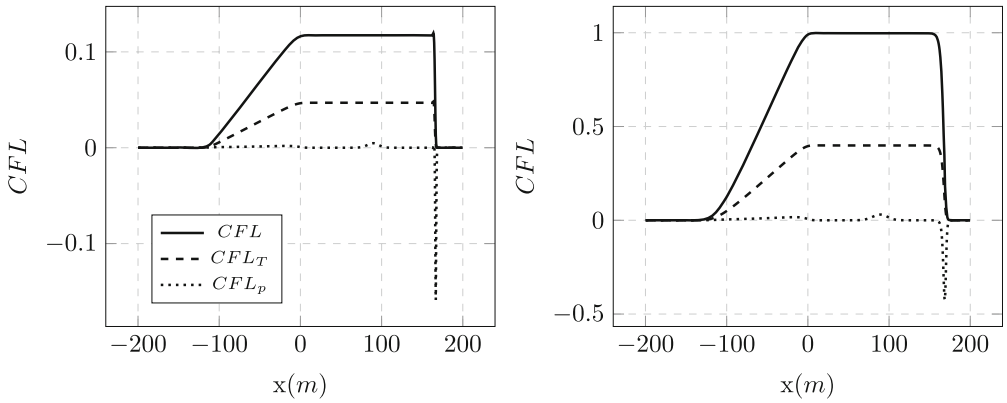

FIGURE 14 CFL_x numbers for the SOD case for two different velocity based *CFL* simulations with $\theta = 1$. Left frame: *CFL* = 0.04. Right frame: *CFL* = 1.0

10970363, 2022, 12, Downloaded from https://onlinelibrary.wiley.com/doi/10.1002/fld.5116 by Jozef Stefan Institute, Wiley Online Library on [07/04/2025]. See the Terms and Conditions (https://onlinelibrary.wiley.com/terms-and-conditions) on Wiley Online Library for rules of use; OA articles are governed by the applicable Creative Commons License

$L = 0.4603\ m$ is illustrated on the Figure 17. The flow is driven by the lateral walls temperature difference. The mean Nusselt number $\overline{Nu} = \frac{1}{L}\int_{y=0}^{y=L} Nu(y)dy$ evaluated on the cold and hot walls are compared to their referenced values, with:

$$Nu(y) = \frac{L}{(T_h - T_c)}\frac{\lambda}{\lambda_0}\frac{\partial T}{\partial x}\Big|_w(y), \qquad Ra = Pr\frac{g\rho_0^2(T_h - T_c)L^3}{T_0\mu_0^2}.$$

The flow dimensionless variables are: $\hat{p} = p/p_0$, $\hat{u} = u/U_0$, $\hat{v} = v/U_0$, $\hat{T} = (T - T_c)/(T_h - T_c)$, where $U_0 = \alpha_0/L$, with $\alpha_0 = \lambda_0/(\rho_0 C_p)$.

The initial conditions are $p_0 = 10.1325 \times 10^4$ Pa and $T_0 = 600$ K. The boundary conditions are $T_h = 960$ K and $T_c = 240$ K on the side walls. Other walls are considered adiabatic. The following fluid properties are constant: $\mu_0 = 1.68 \times 10^{-5}$ kg m^{-1} s^{-1} and $\lambda_0 = \mu_0\gamma R/((1-\gamma)Pr)$, with $Pr = 0.71$ and $R = 287$ J kg^{-1} K^{-1}. All simulations are performed with $\theta = 1$ and 3 subiterations. A sensitivity mesh study is realized and shown in Figure 15B. Beyond 740×740 cells, the Nusselt number have negligible variation. Thus, only results obtained with this mesh (Figure 16B) are discussed. The corresponding time step used is $\Delta t = 0.0025$ s. The steady state is reached after approximately 10 s of simulations

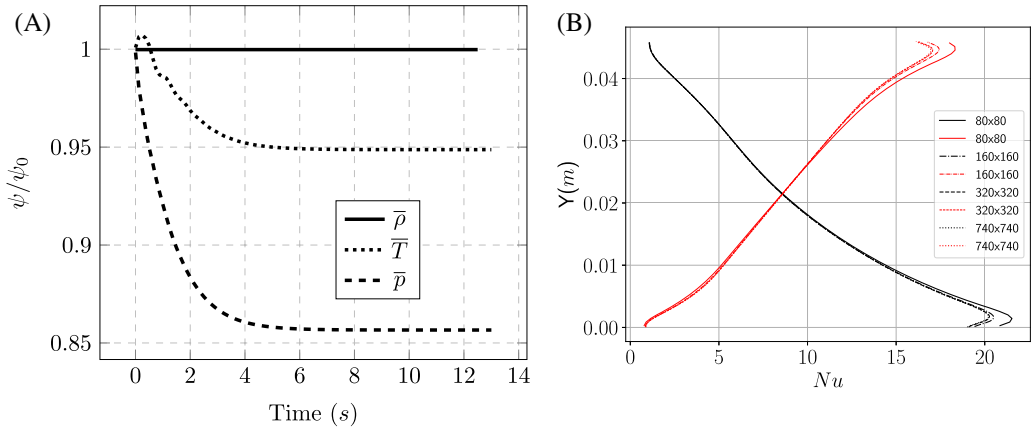

FIGURE 15 (A) Relative domain-averaged quantities ψ/ψ_0 over time (B) Nusselt number over the nonadiabatic walls for different mesh refinements; the hot and cold walls are represented by red and black lines, respectively [Colour figure can be viewed at wileyonlinelibrary.com]

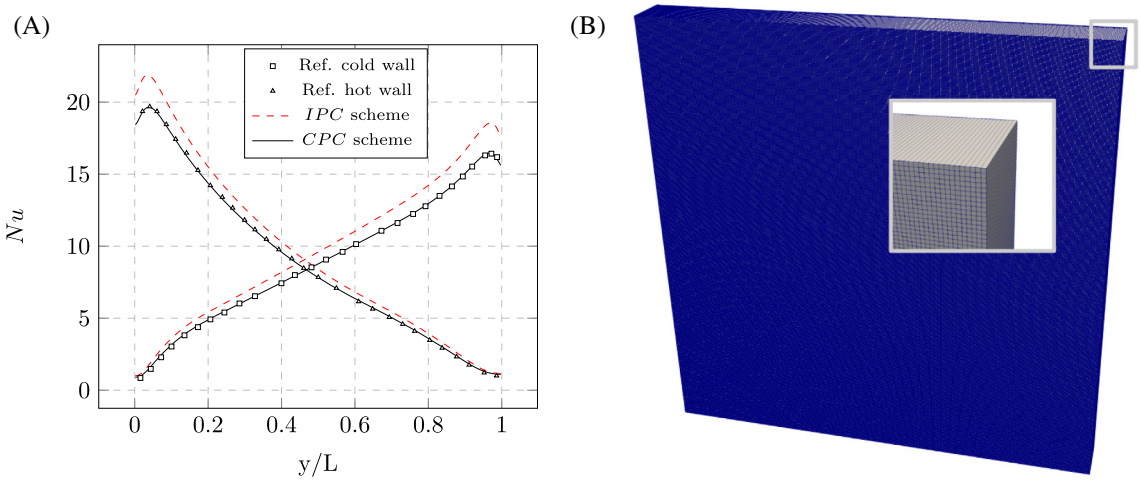

FIGURE 16 (A) Nusselt number profiles for the hot and cold walls compared to the IPC[46] scheme and that of Reference 60. (B) 740×740 cells hexahedral mesh used for the presented results [Colour figure can be viewed at wileyonlinelibrary.com]

10970363, 2022, 12, Downloaded from https://onlinelibrary.wiley.com/doi/10.1002/fld.5116 by Jozef Stefan Institute, Wiley Online Library on [07/04/2025]. See the Terms and Conditions (https://onlinelibrary.wiley.com/terms-and-conditions) on Wiley Online Library for rules of use; OA articles are governed by the applicable Creative Commons License

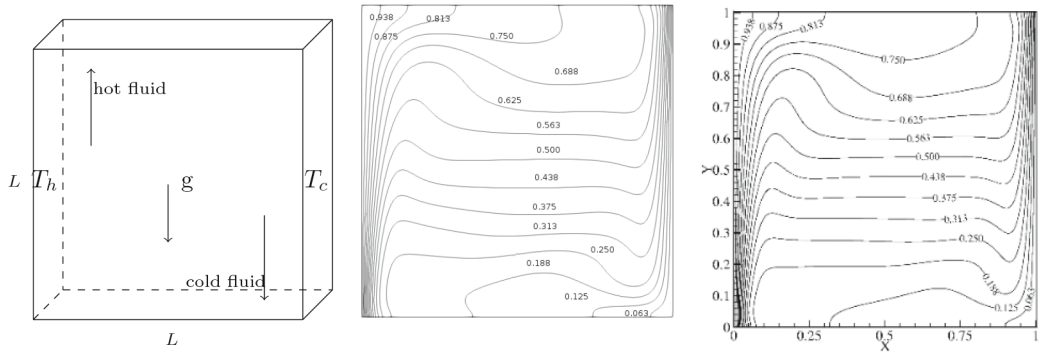

FIGURE 17 Left: sketch of the system. Centre: steady state dimensionless temperature $\hat{t}$ iso-contours. Right: steady state dimensionless temperature $\hat{t}$ iso-contours, reference from Reference 60

TABLE 4 Comparison between the mean Nusselt numbers and total pressure ratio with the reference values from Reference 58. Results from the mesh simulation of a converged 740 × 740 cells

	Present CPC scheme	IPC scheme[46]	Reference 58
$\overline{Nu}_w$	9.7	8.86	8.86
$\hat{p}$	1.000	0.856	0.856

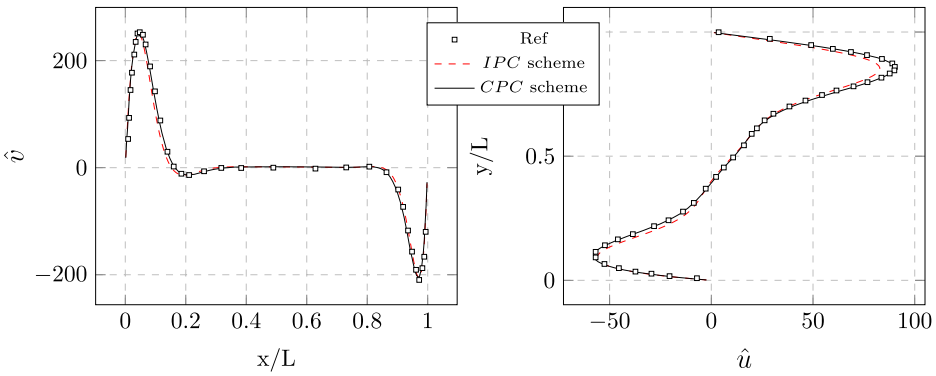

FIGURE 18 Distribution of the velocity on the centerlines of the convective cavity compared to Reference 60 [Colour figure can be viewed at wileyonlinelibrary.com]

(Figure 15A). Note that the mean cavity density remains constant over time, while the other thermodynamic fields converge to their steady solutions. Figure 17 compares some temperature iso-contours over the cavity for the presented algorithm to the reference results,[60] which are very similar. Table 4 compares the CPC and IPC schemes steady results against Reference 58. The pressure variation is well reproduced by the CPC algorithm in the heated cavity, where its mean value reaches the expected reference value of 0.856. This is not the case for the IPC scheme due to the lack of pressure variation. Moreover, the mean Nusselt numbers of both walls are in agreement with their expected values of 8.86 (see Figure 16A) for the Nusselt number profiles over the two given walls). This is directly linked to the correct shape of the vertical and horizontal velocity profiles over the cavity, as shown in Figure 18. As observed in the pressure cooker test case (3.1), the present comparison clearly shows that the thermodynamic pressure variation and wall heat fluxes are well reproduced.

In conclusion, the simulation results show that the proposed scheme can be as accurate as other numerical methods,[59,61-63] which are known to predict correct natural convection solutions.

10970363, 2022, 12, Downloaded from https://onlinelibrary.wiley.com/doi/10.1002/fld.5116 by Jozef Stefan Institute, Wiley Online Library on [07/04/2025]. See the Terms and Conditions (https://onlinelibrary.wiley.com/terms-and-conditions) on Wiley Online Library for rules of use; OA articles are governed by the applicable Creative Commons License

4 | LOCK EXCHANGE CASE

This case focuses on a two dimensional gravity current flow in a lock exchange configuration. The system is a rectangular cavity of height 2L and width 30L, with $L = 1\ m$ the half-height of the cavity (see Figure 19 for the system sketch). The temperature difference $\Delta T = 2\ K$ between the heavy and light fluids, respectively at T_c (on the right) and T_h (on the left), drives the flow. The top and bottom walls have the no slip condition and others boundaries are treated as symmetries.

The Grashof number describing the flow is $Gr = \frac{g\beta\Delta TL^3}{\nu^2} = 1.25.10^6$, and the dimensionless time is denoted by $t^+ = \frac{tU}{L}$, where $U = \sqrt{\beta\Delta TgL}$ and $\beta = 2/(T_h + T_c)$. An LES simulation is performed using a mesh with 768×91 cells based on the reference paper,[64] with $\Delta t = 0.017$ s. 2 inner-iterations where used and $\theta = 1/2$. The numerical density iso contours (10 contours linearly separated from the minimum and maximum densities) at $t^+ = 10$ and 20 are compared with the 2D DNS reference results.[64]

The results presented in Figure 20 show a good agreement between the CPC scheme LES simulation and the reference DNS density iso contours, where symmetric structures can be observed induced by the buoyant flow effects.

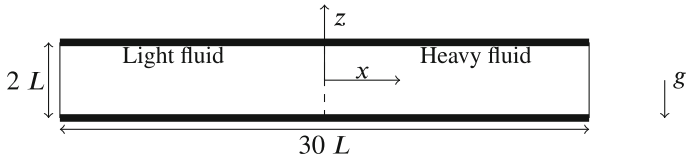

FIGURE 19 Sketch of the lock exchange system

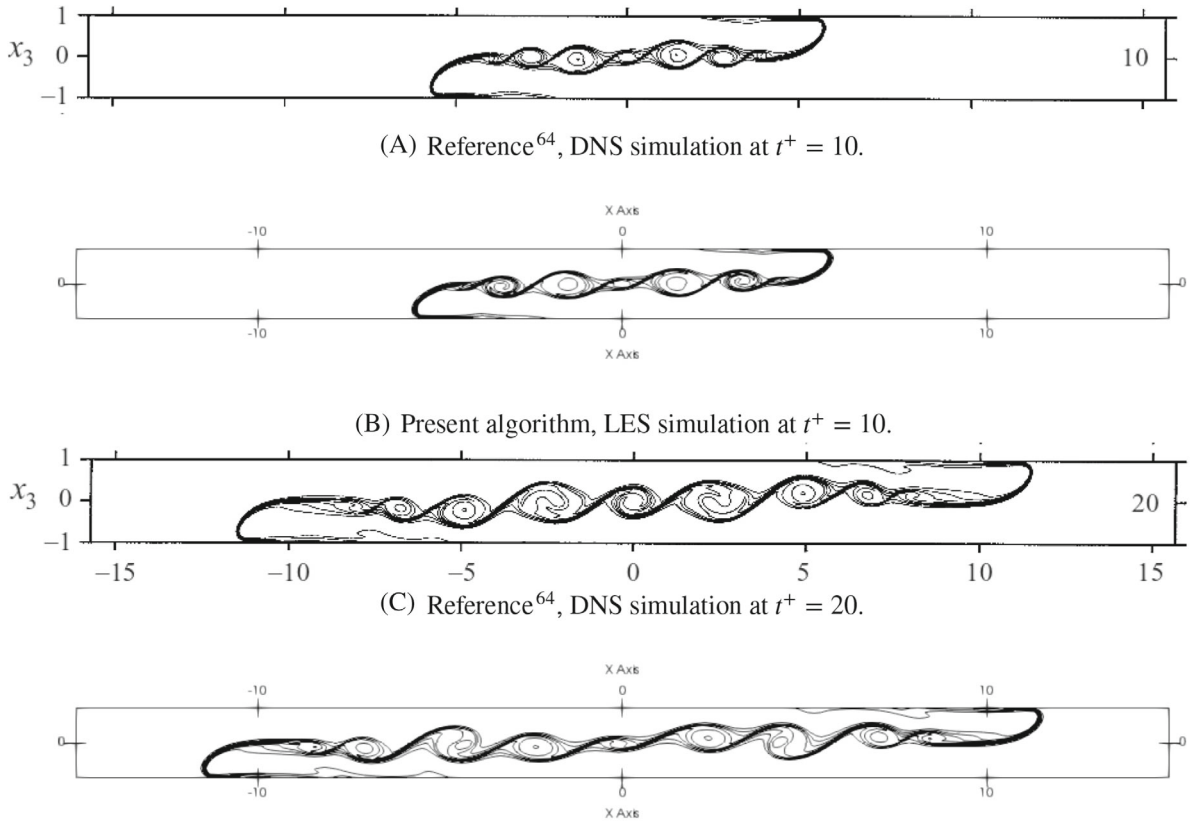

(A) Reference[64], DNS simulation at $t^+ = 10$.

(B) Present algorithm, LES simulation at $t^+ = 10$.

(C) Reference[64], DNS simulation at $t^+ = 20$.

(D) Present algorithm, LES simulation at $t^+ = 20$.

FIGURE 20 Lock exchange system density iso contours at two values of t^+

10970363, 2022, 12, Downloaded from https://onlinelibrary.wiley.com/doi/10.1002/fld.5116 by Jozef Stefan Institute, Wiley Online Library on [07/04/2025]. See the Terms and Conditions (https://onlinelibrary.wiley.com/terms-and-conditions) on Wiley Online Library for rules of use; OA articles are governed by the applicable Creative Commons License

This emphasizes the ability of the proposed algorithm to reproduce different types of flows, from the compressible to the incompressible limit. Note that this type of flow could not be correctly reproduced by an isentropic pressure correction compressible scheme.

5 | LES SIMULATION ON A 3-D VENTILATED ROOM

Finally, the CPC scheme is tested on a more complex validation case, the MINIBAT[65] configuration, whose 3-D flow is driven by a turbulent axisymmetrical jet. The numerical results were compared with the experimental data.[66] Even if the $3.1 \times 3.1 \times 2.5$ m^3 system geometry (shown in Figure 21) appears simple, several studies have shown the difficulty in predicting the flow mean and instantaneous quantities.[67,68] Two RANS simulations, using the $k - \varepsilon$ and R_{ij} approaches were compared to a LES simulation. A radial interpolation on the velocity, temperature, and turbulent kinetic energy at

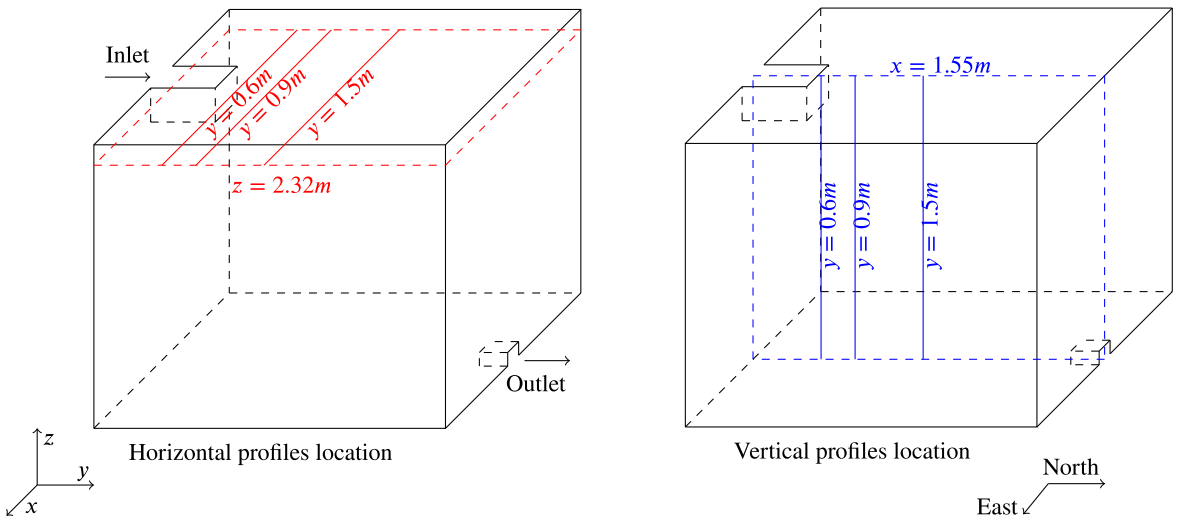

FIGURE 21 Location of the horizontal and vertical line segments where the numerical and experimental results are compared [Colour figure can be viewed at wileyonlinelibrary.com]

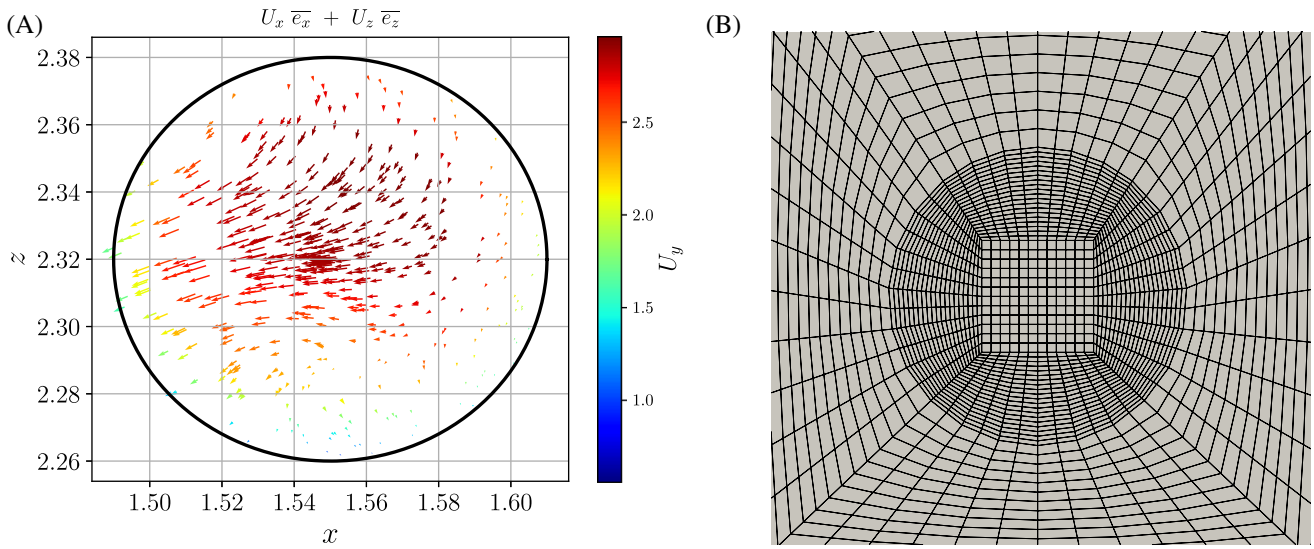

FIGURE 22 (A) Interpolated velocity field for the inlet boundary condition (B) hexahedral mesh used for the simulations [Colour figure can be viewed at wileyonlinelibrary.com]

10970363, 2022, 12, Downloaded from https://onlinelibrary.wiley.com/doi/10.1002/fld.5116 by Jozef Stefan Institute, Wiley Online Library on [07/04/2025]. See the Terms and Conditions (https://onlinelibrary.wiley.com/terms-and-conditions) on Wiley Online Library for rules of use; OA articles are governed by the applicable Creative Commons License

TABLE 5 Wall boundary conditions

Wall	South	North	East	West	Ceiling	Floor
Temperature (K)	295.6	295.6	295.5	295.5	295.6	295.7

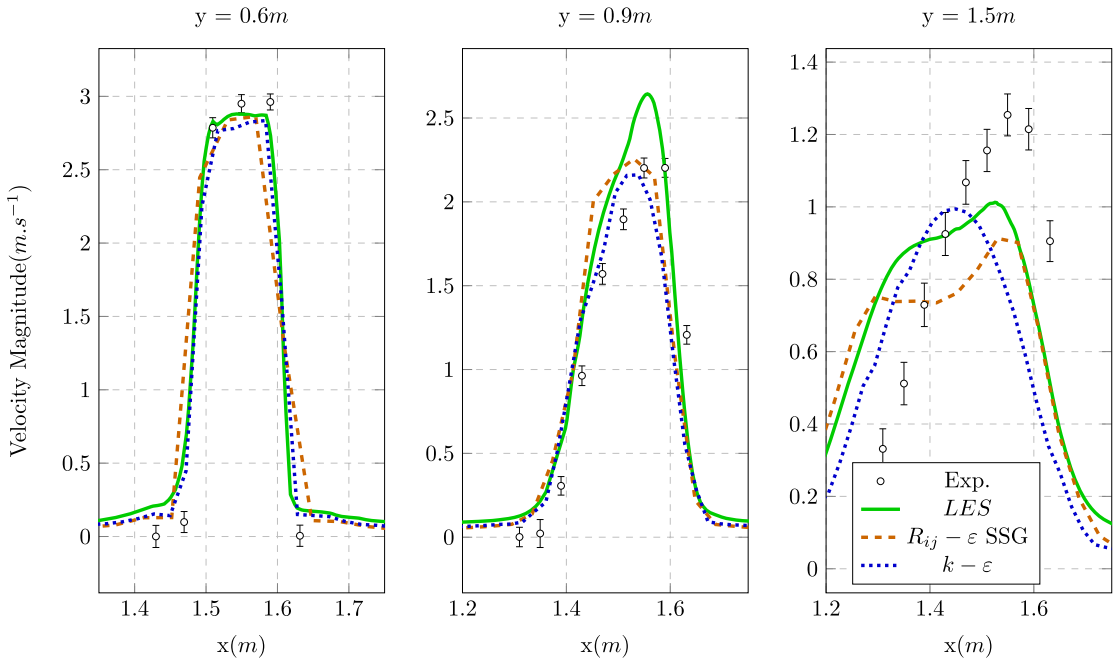

FIGURE 23 Profiles of the velocity magnitude at the horizontal line segments for different turbulent simulations [Colour figure can be viewed at wileyonlinelibrary.com]

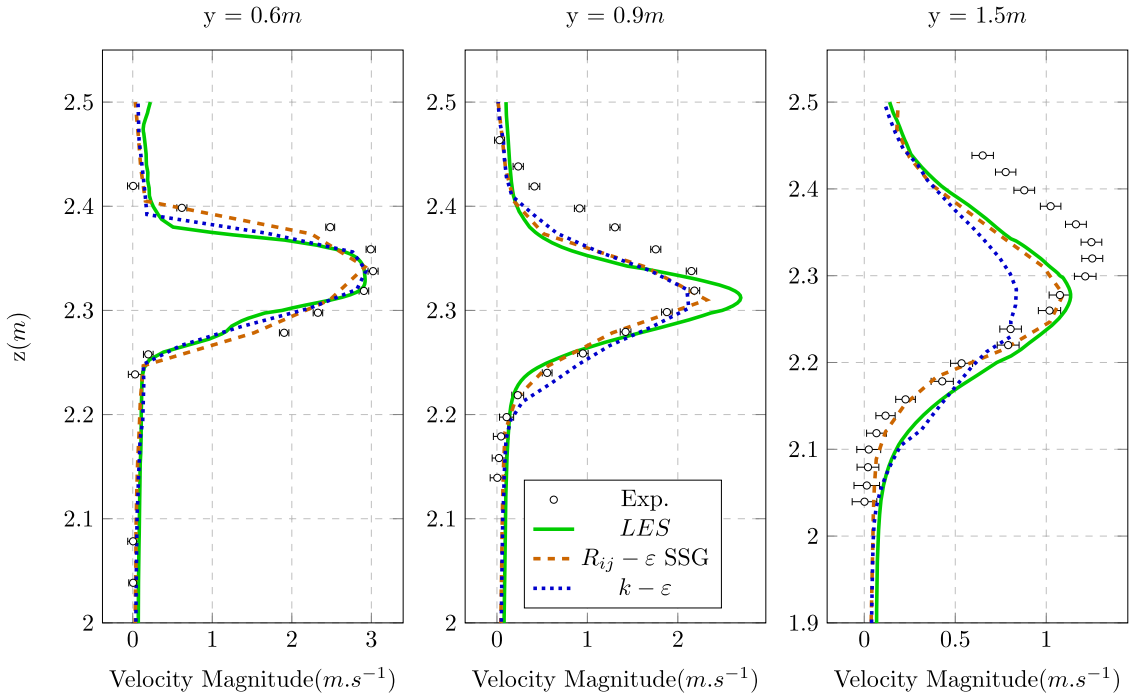

FIGURE 24 Profiles of the velocity magnitude at the vertical line segments for different turbulent simulations [Colour figure can be viewed at wileyonlinelibrary.com]

10970363, 2022, 12, Downloaded from https://onlinelibrary.wiley.com/doi/10.1002/fld.5116 by Jozef Stefan Institute, Wiley Online Library on [07/04/2025]. See the Terms and Conditions (https://onlinelibrary.wiley.com/terms-and-conditions) on Wiley Online Library for rules of use; OA articles are governed by the applicable Creative Commons License

the inlet faces based on the experimental data is performed. The mean inlet velocity and temperature are $V_{in} = 2.96$ m s^{-1} and $T_{in} = 294.95$ K. The resulting 2-D inlet interpolated velocity field is shown in Figure 22A. One can see that as a direct consequence of the experimental inlet duct, the flow deviates along the x axis, making the jet nonsymmetric. The no-slip wall Dirichlet boundary conditions are listed in Table 5.

More information about the configuration and its experiment conditions can be found in References 66 and 65. A hexahedral mesh composed of 7.5 million cells was used for the simulations (Figure 22B); for RANS computations, $\theta = 1$ and for the LES simulation, $\theta = 1/2$. Two inner-iterations are performed for each time step, fixed to $\Delta t = 0.0025$ s. Once a statistical steady state was reached in LES, the main fields were averaged for 30 s. The velocity magnitude and diagonal

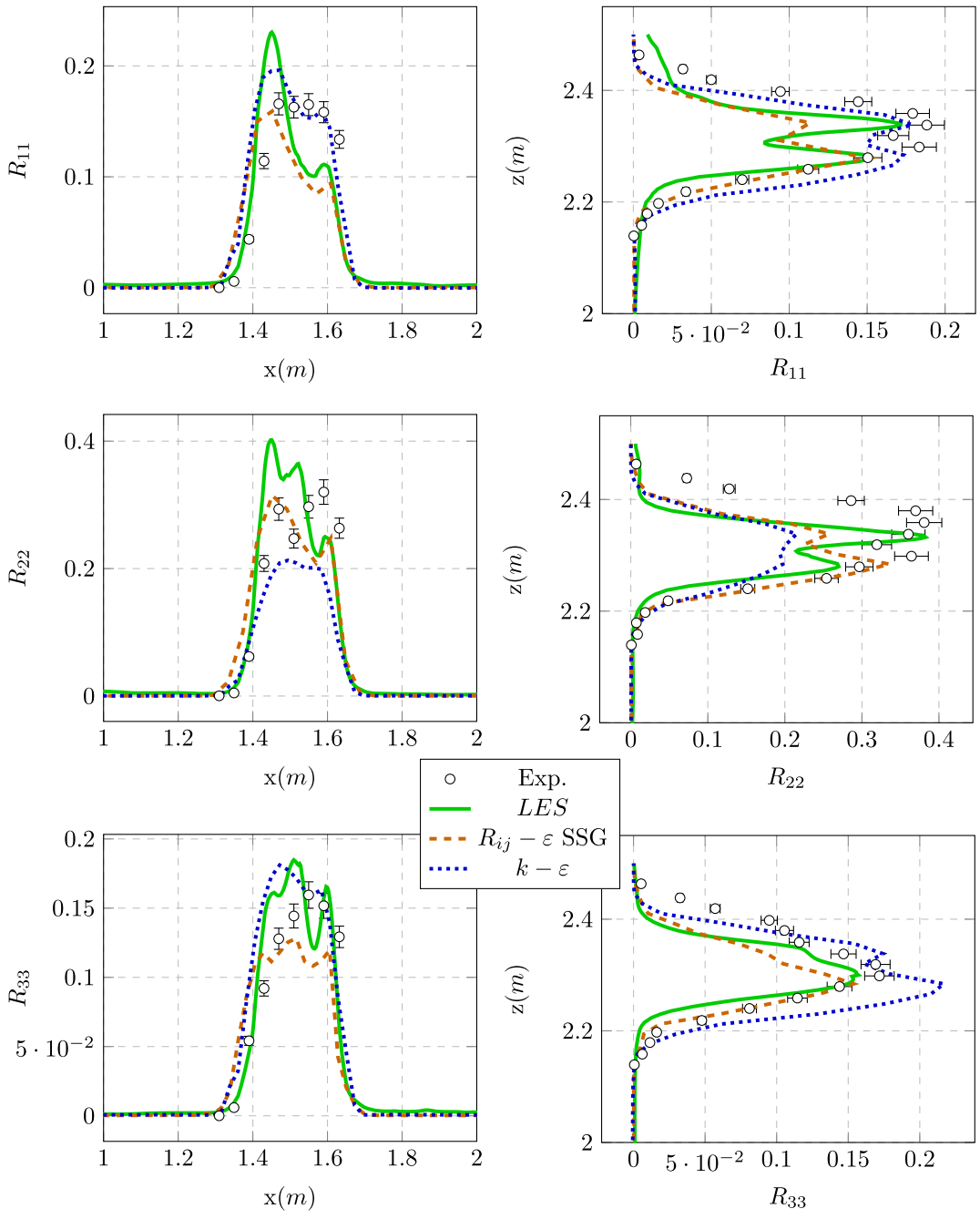

FIGURE 25 (A–C) Horizontal and (D–F) vertical R_{ii} profiles at $y = 0.9$ m. Legend: (•) Experimental data, (.....) $k - \varepsilon$, (.....) $R_{ij} - \varepsilon$ (SSG), (——) LES [Colour figure can be viewed at wileyonlinelibrary.com]

10970363, 2022, 12, Downloaded from https://onlinelibrary.wiley.com/doi/10.1002/fld.5116 by Jozef Stefan Institute, Wiley Online Library on [07/04/2025]. See the Terms and Conditions (https://onlinelibrary.wiley.com/terms-and-conditions) on Wiley Online Library for rules of use; OA articles are governed by the applicable Creative Commons License

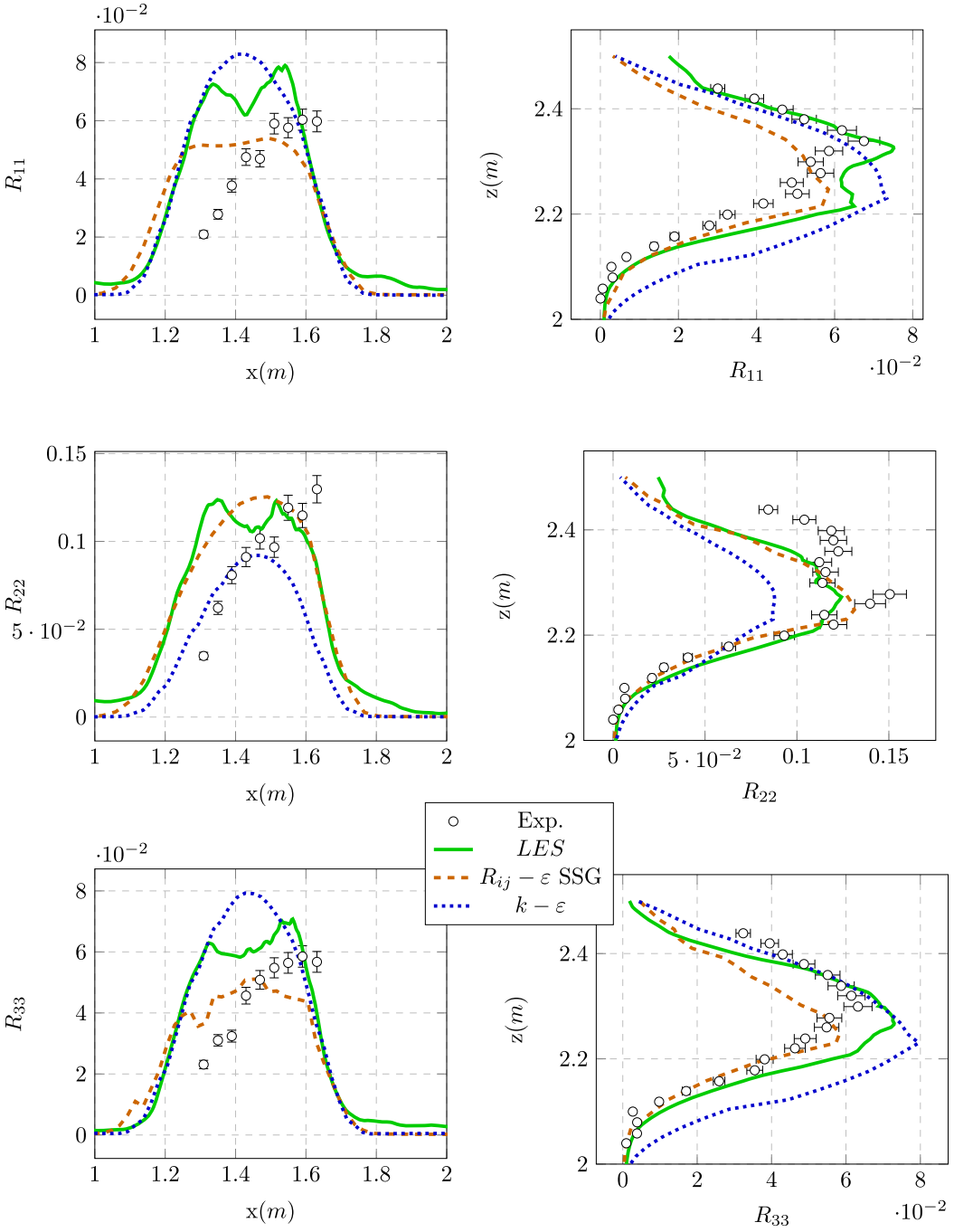

FIGURE 26 (A–C) Horizontal and (D–F) vertical R_{ii} profiles at $y = 1.5$ m. Legend: (•) Experimental data, (- - -) $k - \varepsilon$, (.....) $R_{ij} - \varepsilon$ (SSG), (——) LES [Colour figure can be viewed at wileyonlinelibrary.com]

terms of the Reynolds stress tensor were compared with the experimental values at the different horizontal and vertical line segments presented in Figure 21.

Figure 23 shows the horizontal velocity magnitude profiles as the distance from the jet inlet increases. Near the jet, both numerical and experimental profiles are in agreement and few differences between the different turbulent simulations are observed, which is expected as the fields are interpolated in the inlet. As the axial distance increases, the jet diffusion seems to be over-evaluated by the CPC numerical scheme, for all turbulent approaches. Moreover, the simulations globally do not accurately reproduce the observed jet shift. Similarly, the vertical velocity profiles, shown in Figure 24 present an overestimation of the jet diffusion, even if the velocity profile shapes are similar to that from the

10970363, 2022, 12, Downloaded from https://onlinelibrary.wiley.com/doi/10.1002/fld.5116 by Jozef Stefan Institute, Wiley Online Library on [07/04/2025]. See the Terms and Conditions (https://onlinelibrary.wiley.com/terms-and-conditions) on Wiley Online Library for rules of use; OA articles are governed by the applicable Creative Commons License

experiment. However, the LES simulation leads to more accurate results for higher y values, where a light shift can be observed.

The instantaneous quantities are presented in Figures 25 and 26 for $y = 0.9$ and 1.5 m, respectively. At the $y = 0.9$ m line segment, all $k - \varepsilon$, R_{ij} and LES simulations provided horizontal and vertical results close to the experimental ones. More precisely, one can perceive that the $k - \varepsilon$ simulation is in agreement with the experimental results for the Reynolds stress tensor R_{11} and R_{33} components, whereas the R_{ij} simulation is more precise for the axial component R_{22}. The LES profiles present peaks close the experimental ones for all R_{ii} components. The R_{ij} simulation profiles have the expected shapes but globally underestimate the tensor components. For $y = 1.5$ m, the shift present in the mean velocity magnitude profiles can be noticed, especially for the LES simulation. Moreover, the R_{ij} and *LES* simulations show profiles more in agreement with the experimental data compared to the $k - \varepsilon$ one. Although some error still exist, the cause of which remains to be investigated, the different simulations were able to predict the instantaneous flow quantities with more accuracy than the mean ones. Indeed, even for a consequent distance from the jet inlet, the diagonal Reynolds stress tensor terms were well predicted. Globally, the LES simulation led to the most convincing results; the shapes of the numerical profiles were in agreement with the experimental and the peaks amplitude were correctly reproduced for the two different jet zones. This test case demonstrates the CPC scheme compatibility with both RANS and LES approaches.

6 | CONCLUSIONS

A second-order accurate conservative time scheme for variable-density flow was developed as an extension of the work of Pierce et al.[69] A staggered time variable arrangement is used but for the finite volume discretization. A Helmholtz equation is solved in the correction step. This allows the thermodynamic pressure variation to be considered while avoiding a time-step restriction linked to the acoustic waves. Further, the use of the internal energy equation supplemented with a kinetic energy-based source term, presented by Herbin et al.,[26] was extended for the proposed sub-iterative algorithm architecture. Hence, the shock solutions were well reproduced by simulations. After implementation on the CFD solver code_saturne, the time scheme accuracy and properties were verified and validated against the analytical solutions and experimental values of various compressible and incompressible flows.

First, we showed that the scheme can accurately consider pressure variations while conserving the mass. The second order accuracy was then achieved, and the conservation of mass and momentum were ensured in a one-dimensional convection test case. Moreover, the proposed method provided consistent solutions for regular and irregular shock problems, even for a material velocity-based Courant number. Two new *CFL*-like conditions to ensure the positivity of the pressure, temperature and density were provided and shown to be less constraining than the classical *CFL* condition. For the validation process, a natural convection benchmark case was used, where the scheme provided results in agreement with the reference. A comparison between the presented time algorithm and one using a Poisson equation in the correction step emphasized the importance of considering the thermodynamical pressure during this crucial scheme step in order to reproduce such phenomena correctly. Finally, RANS and LES turbulent simulations were performed on a 3D ventilation geometry, emphasizing the potential of the scheme for industrial problems.

Further work will focus on the extension of the presented algorithm to variable fluid properties, more generic equations of state and applications on more complex industrial applications. In addition, new tests should be conducted at other different Mach number cases.

ACKNOWLEDGMENTS

The first author receives a financial support by ANRT through an EDF-CIFRE contract. All computational facilities were provided by EDF R&D and the CEREA laboratory. The authors thank Jean-Marc Hérard (EDF R&D) and Anne Sergent (LIMSI) for valuable discussions.

ENDNOTE

*Hereafter, the equation of state $T(\rho, e)$ is assumed to be invertible to provide $e(\rho, T)$. Combined with $p(\rho, e)$, the resulting equation of state for pressure—$p(\rho, T)$—is also assumed to be invertible to provide $\varrho(T, p)$ and $\left.\frac{\partial \varrho}{\partial p}\right|_T$.

ORCID

Hector Amino https://orcid.org/0000-0002-6996-8533

10970363, 2022, 12, Downloaded from https://onlinelibrary.wiley.com/doi/10.1002/fld.5116 by Jozef Stefan Institute, Wiley Online Library on [07/04/2025]. See the Terms and Conditions (https://onlinelibrary.wiley.com/terms-and-conditions) on Wiley Online Library for rules of use; OA articles are governed by the applicable Creative Commons License

REFERENCES

1. Ying H, Hong-Gye S, Shih-Yang H, Vigor Y. Large-eddy simulation of combustion dynamics of lean-premixed swirl-stabilized combustor. *J Propuls Power*. 2003;19(5):782-794. doi:10.2514/2.6194
2. Weeratunge M, Ranga Dinesh KKJ, Ibrahim SS, Kirkpatrick MP. Large eddy simulation of isothermal turbulent swirling jets. *Combust Sci Technol*. 2007;179(8):1481-1525. doi:10.1080/00102200701196472
3. Frédéric A, Jean-Marc H, Jérôme L. Comparative study of pressure-correction and Godunov-type schemes on unsteady compressible cases. *Comput Fluids*. 2009;38(8):1495-1509. doi:10.1016/j.compfluid.2008.12.005
4. Alexandre D, Clarisse D, Hervé B, Jean-Bernard G. Numerical modelling of an anodic metal bath heated with an argon transferred arc. *ISIJ Int*. 2003;43(8):1128-1135. doi:10.2355/isijinternational.43.1128
5. Sergiu K, Andrew M. Singular limits of quasilinear hyperbolic systems with large parameters and the incompressible limit of compressible fluids. *Commun Pure Appl Math*. 1981;34(4):481-524. doi:10.1002/cpa.3160340405
6. Hervé G, Cécile V. On the behaviour of upwind schemes in the low Mach number limit. *Comput Fluids*. 1999;28(1):63-86.
7. Degond P, Tang M. All speed scheme for the low Mach number limit of the isentropic Euler equations. *Commun Comput Phys*. 2011;10(1):1-31.
8. Jeffrey H, Shi J, Jian-Guo L. An all-speed asymptotic-preserving method for the isentropic Euler and Navier-Stokes equations. *Communications in Computational Physics*. 2012;12(4):955-980.
9. Floraine C, Pierre D, Anela K. An asymptotic-preserving all-speed scheme for the Euler and Navier–Stokes equations. *J Comput Phys*. 2012;231(17):5685-5704.
10. Walter B, Giacomo D, Raphaël L, Maurizio T, Marie-Hélène V. A second order all Mach number IMEX finite volume solver for the three dimensional Euler equations. *J Comput Phys*. 2020;415:109486.
11. Park JH, Munz C-D. Multiple pressure variables methods for fluid flow at all Mach numbers. *Int J Numer Methods Fluids*. 2005;49(8):905-931.
12. Joel CA. Numerical solution of the Navier-Stokes equations. *Math Comput*. 1968;22(104):745-762. doi:10.2307/2004575
13. Roger T. Sur l'approximation de la solution des équations de Navier-Stokes par la méthode des pas fractionnaires (I). *Arch Ration Mech Anal*. 1969;32(2):135-153. doi:10.1007/BF00247678
14. Jean-Luc G, Peter M, Jie S. An overview of projection methods for incompressible flows. *Comput Methods Appl Mech Eng*. 2006;195(44-47):6011-6045. doi:10.1016/j.cma.2005.10.010
15. Harlow Francis H, Amsden AA. Numerical calculation of almost incompressible flow. *J Comput Phys*. 1968;3(1):80-93. doi:10.1016/0021-9991(68)90007-7
16. Harlow Francis H, Amsden AA. A numerical fluid dynamics calculation method for all flow speeds. *J Comput Phys*. 1971;8(2):197-213. doi:10.1016/0021-9991(71)90002-7
17. Demirdžić I, Lilek Ž, Perić M. A collocated finite volume method for predicting flows at all speeds. *Int J Numer Methods Fluids*. 1993;16(12):1029-1050. doi:10.1002/fld.1650161202
18. Moukalled F, Darwish M. A high-resolution pressure-based algorithm for fluid flow at all speeds. *J Comput Phys*. 2001;168(1):101-130. doi:10.1006/jcph.2000.6683
19. Politis ES, Giannakoglou KC. A Pressure-Based Algorithm for high-speed turbo-machinery flows. *Int J Numer Methods Fluids*. 1997;25(1):63-80. doi:10.1002/(SICI)1097-0363(19970715)25
20. Van Doormaal JP, Raithby GD, McDonald BH. The segregated approach to predicting viscous compressible fluid flows; 1987.10.1115/1.3262097
21. Karki KC, Patankar SV. Pressure based calculation procedure for viscous flows at all speeds in arbitrary configurations. *AIAA J*. 1989;27(9):1167-1174. doi:10.2514/3.10242
22. Issa RI. Solution of the implicitly discretised fluid flow equations by operator-splitting. *J Comput Phys*. 1986;62(1):40-65. doi:10.1016/0021-9991(86)90099-9
23. Issa Raad I, Gosman AD, Watkins AP. The computation of compressible and incompressible recirculating flows by a non-iterative implicit scheme. *J Comput Phys*. 1986;62(1):66-82. doi:10.1016/0021-9991(86)90100-2
24. Phillip C, Karen P. A projection method for low speed flows. *J Comput Phys*. 1999;149(2):245-269. doi:10.1006/jcph.1998.6152
25. Heul Duncan R, Cornelis V, Piet W. A conservative pressure-correction method for flow at all speeds. *Comput Fluids*. 2003;32(8):1113-1132. doi:10.1016/S0045-7930(02)00086-5
26. Raphaèle H, Jean-Claude L, Chady Z. A cell-centred pressure-correction scheme for the compressible Euler equations. *IMA J Numer Anal*. 2020;40(3):1792-1837. doi:10.1093/imanum/drz024
27. Harlow Francis H, Eddie WJ. Numerical calculation of time-dependent viscous incompressible flow of fluid with free surface. *Phys Fluids*. 1965;8(12):2182-2189. doi:10.1063/1.1761178
28. Crank J, Nicolson P. A practical method for numerical evaluation of solutions of partial differential equations of the heat-conduction type; 1947:50-67; Cambridge University Press.
29. Pierce Charles D, Parviz M. Progress-variable approach for large-eddy simulation of non-premixed turbulent combustion. *J Fluid Mech*. 2004;504:73. doi:10.1017/S0022112004008213
30. Clifton W, Pierce Charles D, Parviz M. A semi-implicit method for resolution of acoustic waves in low Mach number flows. *J Comput Phys*. 2002;181(2):545-563. doi:10.1006/jcph.2002.7141
31. Tommaso B, Rupert K. A semi-implicit compressible model for atmospheric flows with seamless access to soundproof and hydrostatic dynamics. *Mon Weather Rev*. 2019;147(11):4221-4240. doi:10.1175/MWR-D-19-0073.1

10970363, 2022, 12, Downloaded from https://onlinelibrary.wiley.com/doi/10.1002/fld.5116 by Jozef Stefan Institute, Wiley Online Library on [07/04/2025]. See the Terms and Conditions (https://onlinelibrary.wiley.com/terms-and-conditions) on Wiley Online Library for rules of use; OA articles are governed by the applicable Creative Commons License

32. Vincent M, Claude B, Heinz P. An efficient semi-implicit compressible solver for large-eddy simulations. *J Comput Phys*. 2007;226(2):1256-1270. doi:10.1016/j.jcp.2007.05.035
33. Olivier D, Guillaume B, Guillaume B, Heinz P. High order conservative finite difference scheme for variable density low Mach number turbulent flows. *J Comput Phys*. 2008;227(15):7125-7159. doi:10.1016/j.jcp.2008.03.027
34. Ascher Uri M, Ruuth Steven J, Spiteri RJ. Implicit-explicit Runge-Kutta methods for time-dependent partial differential equations. *Appl Numer Math*. 1997;25(2-3):151-167.
35. Lorenzo P, Giovanni R. Implicit–explicit Runge–Kutta schemes and applications to hyperbolic systems with relaxation. *J Sci Comput*. 2005;25(1):129-155.
36. Georgij B, Mária L-M, Leonid Y. Asymptotic preserving IMEX finite volume schemes for low Mach number Euler equations with gravitation. *J Comput Phys*. 2017;335:222-248.
37. Walter B, Lorenzo P. High order pressure-based semi-implicit IMEX schemes for the 3D Navier-Stokes equations at all Mach numbers. *J Comput Phys*. 2021;434:110206.
38. Kaarle VH, Weeratunge M. *An Introduction to Computational Fluid Dynamics: the Finite Volume Method*. Pearson Education; 2007.
39. Toro EF. *Riemann Solvers and Numerical Methods for Fluid Dynamics: A Practical Introduction*. Springer Science & Business Media; 2013.
40. Frédéric A, Namane M, Marc S. Code Saturne: a finite volume code for the computation of turbulent incompressible flows-Industrial applications. *Int J Finite Vol*. 2004;1(1). doi:10.1016/j.compfluid.2008.12.005
41. Marie-Charlotte G, Sofiane B, Pierre-Bernard B. Wall-modeled large eddy simulation of the flow through PWR fuel assemblies at Re H= 66 000—Validation on CALIFS experimental setup. *Nucl Technol*. 2020;206(2):255-265. doi:10.1080/00295450.2019.1642684
42. Defforge Cécile L, Bertrand C, Marc B, Raphaël B, Patrick A. Improving numerical dispersion modelling in built environments with data assimilation using the iterative ensemble Kalman smoother. *Bound-Layer Meteorol*. 2021;179(2):209-240. doi:10.1007/s10546-020-00588-9
43. Maya M, Bertrand C. Numerical simulations of pollutant dispersion in an idealized urban area, for different meteorological conditions. *Bound-Layer Meteorol*. 2007;122(2):321-342. doi:10.1007/s10546-006-9110-4
44. Martin F, Harris JC. Finite volume arbitrary Lagrangian-Eulerian schemes using dual meshes for ocean wave applications. *Comput Fluids*. 2021;219:104860. doi:10.1016/j.compfluid.2021.104860
45. Xingsi H, Morgans AS. Simulation of the flame describing function of a turbulent premixed flame using an open-source LES solver. *Combust Flame*. 2015;162(5):1778-1792. doi:10.1016/j.combustflame.2014.11.039
46. Li M, Fatiha N, Jean-Louis C. Verification and validation of a variable–density solver for fire safety applications. *Numer Heat Transf B Fund*. 2019;76(3):107-129. doi:10.1080/10407790.2019.1647721
47. Clément C, Martin F, Jean-Marc H, Jean-Claude L, Erwan LC. An implicit integral formulation to model inviscid fluid flows in obstructed media. *Comput Fluids*. 2019;188:136-163. doi:10.1016/j.compfluid.2019.05.014
48. Edward LB, Sharma Bahrat I. Application of the energy-dissipation model of turbulence to the calculation of flow near a spinning disc. *Lett Heat Mass Transf*. 1974;1(2):131-137. doi:10.1016/0094-4548(74)90150-7
49. Shir CC. A preliminary numerical study of atmospheric turbulent flows in the idealized planetary boundary layer. *J Atmos Sci*. 1973;30(7):1327-1339. doi:10.1175/1520-0469
50. Speziale Charles G, Sutanu S, Gatski TB. Modelling the pressure–strain correlation of turbulence: an invariant dynamical systems approach. *J Fluid Mech*. 1991;227:245-272. doi:10.1017/S0022112091000101
51. Joseph S. General circulation experiments with the primitive equations: I. *Basic Exp Monthly Weather Rev*. 1963;91(3):99-164. doi:10.1175/1520-0493
52. Lilly DK. A proposed modification of the Germano subgrid-scale closure method. *Phys Fluids A Fluid Dyn*. 1992;4(3):633-635. doi:10.1063/1.858280
53. Robert E, Thierry G, Cindy G, Raphaèle H, Roland M. TP or not TP, that is the question. *Comput Geosci*. 2014;18(3-4):285-296. doi:10.1007/s10596-013-9392-9
54. Martin F, Jacques F, Ophélie A. *An Anisotropic Diffusion Finite Volume Algorithm Using a Small Stencil*. Springer; 2014:577-585.
55. Rhie CM, Li CW. Numerical study of the turbulent flow past an airfoil with trailing edge separation. *AIAA J*. 1983;21(11):1525-1532. doi:10.2514/3.8284
56. Fromm JE. A method for reducing dispersion in convective difference schemes. *J Comput Phys*. 1968;3(2):176-189.
57. Sod GA. A survey of several finite difference methods for systems of nonlinear hyperbolic conservation laws. *J Comput Phys*. 1978;27(1):1-31. doi:10.1016/0021-9991
58. Patrick LQ, Catherine W, Henri P, et al. Modelling of natural convection flows with large temperature differences: a benchmark problem for low Mach number solvers. Part 1. Reference solutions. *ESAIM Math Model Numer Anal*. 2005;39(3):609-616. doi:10.1051/m2an:2005027
59. Jan V, Kris R, Erik D. A multigrid semi-implicit line-method for viscous incompressible and low-Mach-number flows on high aspect ratio grids. *J Comput Phys*. 1999;154(2):310-341. doi:10.1006/jcph.1999.6315
60. Masoud D, Seyed-Farid H. Numerical simulation of thermobuoyant flow with large temperature variation. *J Thermophys Heat Transf*. 2006;20(2):285-296. doi:10.2514/1.15804
61. Roland B, Malte B, Rolf R. Numerical simulation of laminar flames at low Mach number by adaptive finite elements. *Comb Theory Model*. 1999;3:503-534. doi:10.1088/1364-7830/3/3/305
62. Le Quéré P, Masson R, Perrot P. A Chebyshev collocation algorithm for 2D non-Boussinesq convection. *J Comput Phys*. 1992;103(2):320-335. doi:10.1016/0021-9991(92)90404-M
63. Patrick LQ, Catherine W, Henri P, et al. Modelling of natural convection flows with large temperature differences: a benchmark problem for low mach number solvers. Part 1. Reference solutions; 2005:39. 10.1051/m2an:2005027

10970363, 2022, 12, Downloaded from https://onlinelibrary.wiley.com/doi/10.1002/fld.5116 by Jozef Stefan Institute, Wiley Online Library on [07/04/2025]. See the Terms and Conditions (https://onlinelibrary.wiley.com/terms-and-conditions) on Wiley Online Library for rules of use; OA articles are governed by the applicable Creative Commons License

64. Carlos H, Eckart M, Frieder N. Analysis and direct numerical simulation of the flow at a gravity-current head. Part 1. flow topology and front speed for slip and no-slip boundaries. *J Fluid Mech*. 2000;418:189-212. doi:10.1017/S0022112000001221
65. Frédéric K. Etude expérimentale des jets axisymétriques anisothermes horizontaux se développant près d'une paroi. Application à la modélisation numérique des cavités ventilées. INSA, Lyon; 2005.
66. Teddy G, Lucie M, Frédéric K. Detailed airflow dynamics and temperature data of axisymmetric and anisothermal jets developing in a room. *Data Brief*. 2020;29:105382. doi:10.1016/j.dib.2020.105382
67. Frédéric K, Gilles R, Raluca H. Experimental and numerical study of a mechanically ventilated enclosure with thermal effects. *Energ Buildings*. 2006;38(8):931-938.
68. Frederic K, Gilles R, Jean B. Experimental and numerical study of a full scale ventilated enclosure: comparison of four two equations closure turbulence models. *Build Environ*. 2007;42(3):1043-1053.
69. Clifton W, Charles P, Parviz M. A method for large eddy simulation of acoustic combustion instabilities; 2003.

How to cite this article: Amino H, Flageul C, Benhamadouche S, Tiselj I, Carissimo B, Ferrand M. A time-staggered second order conservative time scheme for variable density flow. *Int J Numer Meth Fluids*. 2022;94(12):1964-1995. doi: 10.1002/fld.5116

APPENDIX A. KINETIC ENERGY DISCRETE EQUATION

In this section, the source term $\Gamma_c^{u^2/2}\Big|_n^{n+1,k}$ expression is detailed. To do so, the discrete kinetic energy equation was written. The following methodology, based on Reference 26, extends the utilization of a source term in the internal energy equation to time-staggered schemes using sub-iterations. The time scheme architecture implies that the source term used in the buoyant step in the temperature equation at time step $n+1, k+1$ is calculated after the corrective step at time step $n+1, k$. Thus, for the sake of simplicity, we consider $k > 1$ and the Euler equations for this section. The mass flux at a given face is denoted by $\dot{M}_f = \underline{q}_f \cdot \underline{S}_f$ and its positive and negative face contributions $\dot{M}_f^+ = \max(\dot{M}_f, 0)$ and $\dot{M}_f^- = \min(\dot{M}_f, 0)$. The momentum equation is solved between the time steps $[n-1+\theta; n+\theta, k]$:

$$\Omega_c \frac{\Theta\left(\rho_c^n,\, \rho_c^{n+1,k-1}\right)\widetilde{\underline{u}}_c^k - \Theta\left(\rho_c^{n-1},\, \rho_c^{n,k-1}\right)\underline{u}_c^{n-1+\theta}}{\Delta t} + \sum_{f\in\mathcal{F}_c}\left\langle \Theta\left(\underline{u}^{n-1+\theta},\, \widetilde{\underline{u}}^k\right)\right\rangle_f \dot{M}_f\Big|_{n-1+\theta}^{n+\theta,k-1} + \Omega_c \underline{\mathrm{Grad}}_c\left(\left\langle p\Big|_{n-1+\theta}^{n+\theta,k-1}\right\rangle_f\right) = \underline{0}. \tag{A1}$$

The mass equation between the time steps $[n-1+\theta; n+\theta, k-1]$ is multiplied by $\widetilde{\underline{u}}_c^k$:

$$\Omega_c \widetilde{\underline{u}}_c^k \frac{\Theta\left(\rho_c^n,\, \rho_c^{n+1,k-1}\right) - \Theta\left(\rho_c^{n-1},\, \rho_c^{n,k-1}\right)}{\Delta t} + \sum_{f\in\mathcal{F}_c} \widetilde{\underline{u}}_c^k \dot{M}_f\Big|_{n-1+\theta}^{n+\theta,k-1} = 0. \tag{A2}$$

(A1)–(A2) reads:

$$\Theta\left(M_c^{n-1},\, M_c^{n,k-1}\right)\frac{\widetilde{\underline{u}}_c^k - \underline{u}_c^{n-1+\theta}}{\Delta t} + \sum_{f\in\mathcal{F}_c}\left(\left\langle \Theta\left(\underline{u}^{n-1+\theta},\, \widetilde{\underline{u}}^k\right)\right\rangle_f - \widetilde{\underline{u}}_c^k\right)\dot{M}_f\Big|_{n-1+\theta}^{n+\theta,k-1} + \Omega_c \underline{\mathrm{Grad}}_c\left(\left\langle p\Big|_{n-1+\theta}^{n+\theta,k-1}\right\rangle_f\right) = 0. \tag{A3}$$

Multiplying equation (A3) by $\widetilde{\underline{u}}_c^k$ and using $(a-b)a = \frac{a^2-b^2}{2} + \frac{|a-b|^2}{2}$:

$$\Theta\left(M_c^{n-1},\, M_c^{n,k-1}\right)\frac{|\widetilde{\underline{u}}_c^k|^2 - |\underline{u}_c^{n-1+\theta}|^2}{2\Delta t} + \Theta\left(M_c^{n-1},\, M_c^{n,k-1}\right)\frac{\left|\widetilde{\underline{u}}_c^k - \underline{u}_c^{n-1+\theta}\right|^2}{2\Delta t}$$

10970363, 2022, 12, Downloaded from https://onlinelibrary.wiley.com/doi/10.1002/fld.5116 by Jozef Stefan Institute, Wiley Online Library on [07/04/2025]. See the Terms and Conditions (https://onlinelibrary.wiley.com/terms-and-conditions) on Wiley Online Library for rules of use; OA articles are governed by the applicable Creative Commons License

$$+\sum_{f\in\mathcal{F}_c}\left(\frac{\left|\left\langle\Theta\left(\underline{u}^{n-1+\theta},\widetilde{\underline{u}}^{k}\right)\right\rangle_f\right|^2}{2}-\frac{|\widetilde{\underline{u}}_c^{k}|^2}{2}\right)\dot{M}_f\big|_{n-1+\theta}^{n+\theta,k-1}$$
$$-\sum_{f\in\mathcal{F}_c}\frac{\left|\left\langle\Theta\left(\underline{u}^{n-1+\theta},\widetilde{\underline{u}}^{k}\right)\right\rangle_f-\widetilde{\underline{u}}_c^{k}\right|^2}{2}\dot{M}_f\big|_{n-1+\theta}^{n+\theta,k-1}$$
$$+\Omega_c\underline{\mathrm{Grad}}_c\left(\left\langle p\big|_{n-1+\theta}^{n+\theta,k-1}\right\rangle_f\right)\cdot\widetilde{\underline{u}}_c^{k}=\underline{0}. \tag{A4}$$

Then, the mass equation between the time steps $[n-1+\theta;n+\theta,k-1]$, multiplied by $\frac{1}{2}|\widetilde{\underline{u}}_c^{k}|^2$ is added to (A4), leading to

$$\frac{\Theta\left(M_c^{n},M_c^{n+1,k-1}\right)|\widetilde{\underline{u}}_c^{k}|^2-\Theta\left(M_c^{n-1},M_c^{n,k-1}\right)|\underline{u}_c^{n-1+\theta}|^2}{2\Delta t}$$
$$+\sum_{f\in\mathcal{F}_c}\frac{\left|\left\langle\Theta\left(\underline{u}^{n-1+\theta},\widetilde{\underline{u}}^{k}\right)\right\rangle_f\right|^2}{2}\dot{M}_f\big|_{n-1+\theta}^{n+\theta,k-1}+\Omega_c\underline{\mathrm{Grad}}_c\left(\left\langle p\big|_{n-1+\theta}^{n+\theta,k-1}\right\rangle_f\right)\cdot\widetilde{\underline{u}}_c^{k}=$$
$$-\Theta\left(M_c^{n-1},M_c^{n,k-1}\right)\frac{\left|\widetilde{\underline{u}}_c^{k}-\underline{u}_c^{n-1+\theta}\right|^2}{2\Delta t}+\sum_{f\in\mathcal{F}_c}\frac{\left|\left\langle\Theta\left(\underline{u}^{n-1+\theta},\widetilde{\underline{u}}^{k}\right)\right\rangle_f-\widetilde{\underline{u}}_c^{k}\right|^2}{2}\dot{M}_f\big|_{n-1+\theta}^{n+\theta,k-1}. \tag{A5}$$

The simplified momentum equation is used to replace $\underline{\mathrm{Grad}}_c\left(\left\langle p\big|_{n-1+\theta}^{n+\theta,k-1}\right\rangle_f\right)\cdot\widetilde{\underline{u}}_c^{k}$:

$$\frac{\Theta\left(M_c^{n},M_c^{n+1,k}\right)\underline{u}_c^{n+\theta,k}}{\Delta t}+\Omega_c\underline{\mathrm{Grad}}_c\left(\left\langle p\big|_{n-1+\theta}^{n+\theta,k}\right\rangle_f\right)=\frac{\Theta\left(M_c^{n},M_c^{n+1,k-1}\right)\widetilde{\underline{u}}_c^{k}}{\Delta t}+\Omega_c\underline{\mathrm{Grad}}_c\left(\left\langle p\big|_{n-1+\theta}^{n+\theta,k-1}\right\rangle_f\right). \tag{A6}$$

Taking the square of this and multiplying by $\frac{\Delta t}{2}$:

$$\Omega_c\widetilde{\underline{u}}_c^{k}\cdot\underline{\mathrm{Grad}}_c\left(\left\langle p\big|_{n-1+\theta}^{n+\theta,k-1}\right\rangle_f\right)=\frac{\Omega_c^2\Delta t}{2\Theta\left(M_c^{n},M_c^{n+1,k-1}\right)}\left[\left|\underline{\mathrm{Grad}}_c\left(\left\langle p\big|_{n-1+\theta}^{n+\theta,k}\right\rangle_f\right)\right|^2-\left|\underline{\mathrm{Grad}}_c\left(\left\langle p\big|_{n-1+\theta}^{n+\theta,k-1}\right\rangle_f\right)\right|^2\right]$$
$$+\frac{\left[\Theta\left(M_c^{n},M_c^{n+1,k}\right)\right]^2}{\Theta\left(M_c^{n},M_c^{n+1,k-1}\right)}\frac{|\underline{u}_c^{n+\theta,k}|^2}{2\Delta t}-\Theta\left(M_c^{n},M_c^{n+1,k-1}\right)\frac{|\widetilde{\underline{u}}_c^{k}|^2}{2\Delta t}\Omega_c\frac{\left[\Theta\left(M_c^{n},M_c^{n+1,k}\right)\right]}{\Theta\left(M_c^{n},M_c^{n+1,k-1}\right)}\underline{\mathrm{Grad}}_c\left(\left\langle p\big|_{n-1+\theta}^{n+\theta,k}\right\rangle_f\right)\cdot\underline{u}_c^{n+\theta,k}. \tag{A7}$$

By replacing $\Omega_c\widetilde{\underline{u}}_c^{k}\cdot\underline{\nabla}p\big|_{n-1+\theta}^{n+\theta,k-1}$ in (A5) and multiplying it by $\frac{\Theta\left(M_c^{n},M_c^{n+1,k-1}\right)}{\Theta\left(M_c^{n},M_c^{n+1,k}\right)}$, we obtain

$$\frac{\Theta\left(M_c^{n},M_c^{n+1,k}\right)|\underline{u}_c^{n+\theta,k}|^2}{2\Delta t}-\left[\frac{\Theta\left(M_c^{n},M_c^{n+1,k-1}\right)}{\Theta\left(M_c^{n},M_c^{n+1,k}\right)}+1-1\right]\frac{\Theta\left(M_c^{n-1},M_c^{n,k-1}\right)|\underline{u}_c^{n-1+\theta}|^2}{2\Delta t}$$

10970363, 2022, 12, Downloaded from https://onlinelibrary.wiley.com/doi/10.1002/fld.5116 by Jozef Stefan Institute, Wiley Online Library on [07/04/2025]. See the Terms and Conditions (https://onlinelibrary.wiley.com/terms-and-conditions) on Wiley Online Library for rules of use; OA articles are governed by the applicable Creative Commons License

$$
\begin{aligned}
&+\left[\frac{\Theta\left(M_c^n,\, M_c^{n+1,k-1}\right)}{\Theta\left(M_c^n,\, M_c^{n+1,k}\right)}+1-1\right]\sum_{f\in\mathcal{F}_c}\frac{\left|\left\langle\Theta\left(\underline{u}^{n-1+\theta},\,\tilde{\underline{u}}^{k}\right)\right\rangle_f\right|^2}{2}\dot{M}_f\Big|_{n-1+\theta}^{n+\theta,k-1}\\
&+\Omega_c\underline{\nabla}p_c\Big|_{n-1+\theta}^{n+\theta,k}\cdot\underline{u}_c^{n+\theta,k}\\
&=-\Theta\left(M_c^{n-1},\, M_c^{n,k-1}\right)\frac{\Theta\left(M_c^n,\, M_c^{n+1,k-1}\right)}{\Theta\left(M_c^n,\, M_c^{n+1,k}\right)}\frac{\left|\tilde{\underline{u}}_c^{k}-\underline{u}_c^{n-1+\theta}\right|^2}{2\Delta t}\\
&+\frac{\Theta\left(M_c^n,\, M_c^{n+1,k-1}\right)}{\Theta\left(M_c^n,\, M_c^{n+1,k}\right)}\sum_{f\in\mathcal{F}_c}\frac{\left|\left\langle\Theta\left(\underline{u}^{n-1+\theta},\,\tilde{\underline{u}}^{k}\right)\right\rangle_f-\tilde{\underline{u}}_c^{k}\right|^2}{2}\dot{M}_f\Big|_{n-1+\theta}^{n+\theta,k-1}-\Gamma_c^p\Big|_{n-1+\theta}^{n+\theta,k},
\end{aligned}
\tag{A8}
$$

where:

$$
\Gamma_c^p\Big|_{n-1+\theta}^{n+\theta,k}=\frac{\Omega_c^2\Delta t}{2\Theta\left(M_c^n,\, M_c^{n+1,k}\right)}\left[\left|\underline{\mathrm{Grad}}_c\left(\left\langle p\Big|_{n-1+\theta}^{n+\theta,k}\right\rangle_f\right)\right|^2-\left|\underline{\mathrm{Grad}}_c\left(\left\langle p\Big|_{n-1+\theta}^{n+\theta,k-1}\right\rangle_f\right)\right|^2\right].
\tag{A9}
$$

The discrete kinetic energy equation is then written as:

$$
\begin{aligned}
&\frac{\Theta\left(M_c^n,\, M_c^{n+1,k}\right)|\underline{u}_c^{n+\theta,k}|^2-\Theta\left(M_c^{n-1},\, M_c^{n,k-1}\right)|\underline{u}_c^{n-1+\theta}|^2}{2\Delta t}\\
&+\sum_{f\in\mathcal{F}_c}\frac{\left|\Theta\left(\underline{u}_f^{n-1+\theta},\,\tilde{\underline{u}}_f^{k}\right)\right|^2}{2}\dot{M}_f\Big|_{n-1+\theta}^{n+\theta,k-1}+\Omega_c\underline{\mathrm{Grad}}_c\left(\left\langle p\Big|_{n-1+\theta}^{n+\theta,k}\right\rangle_f\right)\cdot\underline{u}_c^{n+\theta,k}\\
&=-\Gamma_c^p\Big|_{n-1+\theta}^{n+\theta,k}+\Theta\left(M_c^{n-1},\, M_c^{n,k-1}\right)\frac{\Theta\left(M_c^n,\, M_c^{n+1,k-1}\right)}{\Theta\left(M_c^n,\, M_c^{n+1,k}\right)}\frac{\left[|\underline{u}_c^{n-1+\theta}|^2-|\tilde{\underline{u}}_c^{k}-\underline{u}_c^{n-1+\theta}|^2\right]}{2\Delta t}\\
&-\Theta\left(M_c^{n-1},\, M_c^{n,k-1}\right)\frac{|\underline{u}_c^{n-1+\theta}|^2}{2\Delta t}+\sum_{f\in\mathcal{F}_c}\frac{\left|\left\langle\Theta\left(\underline{u}^{n-1+\theta},\,\tilde{\underline{u}}^{k}\right)\right\rangle_f\right|^2}{2}\dot{M}_f\Big|_{n-1+\theta}^{n+\theta,k-1}\\
&+\frac{\Theta\left(M_c^n,\, M_c^{n+1,k-1}\right)}{\Theta\left(M_c^n,\, M_c^{n+1,k}\right)}\sum_{f\in\mathcal{F}_c}\left[\frac{\left|\left\langle\Theta\left(\underline{u}^{n-1+\theta},\,\tilde{\underline{u}}^{k}\right)\right\rangle_f-\tilde{\underline{u}}_c^{k}\right|^2}{2}-\frac{\left|\left\langle\Theta\left(\underline{u}^{n-1+\theta},\,\tilde{\underline{u}}^{k}\right)\right\rangle_f\right|^2}{2}\right]\dot{M}_f\Big|_{n-1+\theta}^{n+\theta,k-1}.
\end{aligned}
\tag{A10}
$$

Two terms compose this discrete equations' right hand side: the kinetic energy dissipation into heat, $\Gamma_c^{u^2/2}\Big|_{n-1+\theta}^{n+\theta,k}$ and the second-order term $\Gamma_c^p\Big|_{n-1+\theta}^{n+\theta,k}$, defined by Equation (A9) and not taken into account in the source term for the sake of implementation and because its value tends to zero as the spatial discretization is refined, as explained in Reference 26.

APPENDIX B. PROPERTIES OF THE SCHEME

B.1 Positivity of the internal energy

The discretized internal energy equation used to calculate the temperature was recalled for $k>1$:

$$
c_v\left[M_c^n\frac{T_c^{n+1,k}-T_c^n}{\Delta t}+\sum_{f\in\mathcal{F}_c}\left(\left\langle\Theta\left(T^n,\, T^{n+1,k}\right)\right\rangle_f-T_c^{n+1,k}\right)\dot{M}_f\Big|_n^{n+1,k-1}\right]
$$

10970363, 2022, 12, Downloaded from https://onlinelibrary.wiley.com/doi/10.1002/fld.5116 by Jozef Stefan Institute, Wiley Online Library on [07/04/2025]. See the Terms and Conditions (https://onlinelibrary.wiley.com/terms-and-conditions) on Wiley Online Library for rules of use; OA articles are governed by the applicable Creative Commons License

$$+\sum_{f\in\mathcal{F}_c}\lambda|\underline{S}_f|\frac{\Theta\left(T_c^n,\,T_c^{n+1,k}\right)-\Theta\left(T_{\tilde{c}}^n,\,T_{\tilde{c}}^{n+1,k}\right)}{d_{c\tilde{c}}}=\Omega_c\mu(S_c^2)^{n+\theta}+\Gamma_c^{u^2/2}\Big|_n^{n+1,k-1}$$
$$-\sum_{f\in\mathcal{F}_\rfloor}\left\langle\Theta\left(p^n,\,p^{n+1,k-1}\right)\underline{u}^{n+\theta,k-1}\right\rangle_f\cdot\underline{S}_f+\Omega_c\underline{u}_c^{n+\theta,k-1}\cdot\underline{\nabla}_c p|_{n-1+\theta}^{n+\theta,k-1}. \tag{B1}$$

The equation (B1) yields a linear system $\underline{\underline{A}}\underline{X}=\underline{B}$, where $\underline{X}=(T_c)_{c\in\{1,\dots,N_{cell}\}}$. Considering a convective upwind scheme, the diagonal matrix $\underline{\underline{A}}$ coefficients are, $\forall c\in\{1,\dots,N_{cell}\}$:

$$A_{cc}=c_v\frac{M_c^n}{\Delta t}+c_v\left[\sum_{f\in\mathcal{F}_c}\theta\dot{M}_f^+\Big|_n^{n+1,k-1}-\dot{M}_f|_n^{n+1,k-1}\right]+\left[\sum_{f\in\mathcal{F}_c}\theta\frac{|\underline{S}_f|\lambda_c}{d}{}_{c\tilde{c}}\right]. \tag{B2}$$

To ensure that these terms are positive and considering the upwind convective scheme, the following sufficient *CFL*-like condition is defined:

$$CFL_{T_1}^+<1,\qquad\text{where }\ CFL_{T_1}^+\coloneqq(1-\theta)\frac{\Delta t}{M_c^n}\sum_{f\in\mathcal{F}_c}\dot{M}_f^+\Big|_n^{n+1,k-1}. \tag{B3}$$

$\forall c,\tilde{c},\in\{1,\dots,N_{cell}\}$ with $c\neq\tilde{c}$, the off-diagonal coefficients are

$$A_{c\tilde{c}}=\theta\dot{M}_f^-\Big|_n^{n+1,k-1}. \tag{B4}$$

Remark 2. If the initial temperatures for all cells are positive, $d>0$, c_v, λ, R_a, and Δt are positive and the condition (B3) is respected, all diagonal terms of the matrix $\underline{\underline{A}}$ are strictly positive. Moreover, all off-diagonal coefficients are negative or null. The diagonal terms are strictly larger than the sum of the modulus of off-diagonal terms. Therefore, A is diagonal dominant and a M-matrix. If for all cells c, B_c is strictly positive, then the solution of the linear system $\underline{X}$ is positive.

The right hand side coefficients are:

$$B_c=c_v\frac{M_c^nT_c^n}{\Delta t}+\mu_c\Omega_c^n(S_c^2)^{n+1}-\sum_{f\in\mathcal{F}_\rfloor}c_v(1-\theta)T_f^n\dot{M}_f|_n^{n+1,k-1}+\Omega_c\underline{u}_c^{n+\theta,k-1}\cdot\underline{\nabla}_c p|_{n-1+\theta}^{n+\theta,k-1}-\sum_{f\in\mathcal{F}_\rfloor}\left[|\underline{S}_f|\lambda_c(1-\theta)\frac{(T_c^n-T_{\tilde{c}}^n)}{d_{c\tilde{c}}}\right]$$
$$-R_a\sum_{f\in\mathcal{F}_c}\left[\Theta\left(T_c^n,\,T_c^{n+1,k-1}\right)\dot{M}_f^+\Big|_n^{n+1,k-1}+\Theta\left(T_{\tilde{c}}^n,\,T_{\tilde{c}}^{n+1,k-1}\right)\dot{M}_f^-\Big|_n^{n+1,k-1}\right].$$

By treating the convective and diffusive terms separately, the RHS coefficients are strictly positive if the following *CFL* and Fourier-like conditions are verified:

$$CFL_{T_2}^+<1,\quad\text{where }\ CFL_{T_2}^+\coloneqq\frac{\Delta t}{M_c^n}\sum_{f\in\mathcal{F}_c}\left[\theta(\gamma-1)\frac{T_c^{n+1,k-1}}{T_c^n}+(1-\theta)\gamma\right]\dot{M}_f^+\Big|_n^{n+1,k-1}-\frac{\Delta t(\gamma-1)\underline{u}_c^{n+\theta,k-1}\cdot\underline{\nabla}_c p|_{n-1+\theta}^{n+\theta,k-1}}{p_c^n}. \tag{B5}$$

$$Fo_T^+<1,\qquad\text{where }\ Fo_T^+\coloneqq\frac{\lambda_c(1-\theta)\Delta t}{c_vM_c^n}\sum_{f\in\mathcal{F}_\rfloor}|\underline{S}_f|. \tag{B6}$$

B.1.1 Positivity of the pressure and density

The Helmholtz equation to solve the pressure increment for an ideal gas is recalled:

$$\frac{\Omega_c p_c^{n+1,k}}{\Delta tR_aT_c^{n+1,k}}-\theta\Delta t\sum_{f\in\mathcal{F}_c}\underline{\nabla}_f p_c^{n+1,k}\cdot\underline{S}_f=\frac{(\rho_c^n-\tilde{\rho}_c)\Omega_c^n}{\Delta t}-\sum_{f\in\mathcal{F}_c}\left\langle\Theta\left(\rho^n,\,\rho^{n+1,k-1}\right)\underline{\tilde{u}}^k+\Delta t\underline{\nabla}_c p|_{n-1+\theta}^{n+\theta,k-1}\right\rangle_f\cdot\underline{S}_f$$
$$+(1-\theta)\Delta t\sum_{f\in\mathcal{F}_c}\underline{\nabla}_f p|_{n-2+\theta}^{n-1+\theta}\cdot\underline{S}_f+\frac{\Omega_c p_c^{n+1,k-1}}{\Delta tR_aT_c^{n+1,k}}. \tag{B7}$$

10970363, 2022, 12, Downloaded from https://onlinelibrary.wiley.com/doi/10.1002/fld.5116 by Jozef Stefan Institute, Wiley Online Library on [07/04/2025]. See the Terms and Conditions (https://onlinelibrary.wiley.com/terms-and-conditions) on Wiley Online Library for rules of use; OA articles are governed by the applicable Creative Commons License

Equation (B7) yields a linear system $\underline{\underline{A}}\underline{X} = \underline{B}$, where $\underline{X} = (p_c^{n+1,k})_{c\in\{1,\dots,N_{cell}\}}$. The diagonal matrix A coefficients are, $\forall c \in \{1, \dots, N_{cell}\}$:

$$A_{cc} = \frac{\Omega_c}{\Delta t R_a T_c^{n+1,k}} + \theta\Delta t \sum_{f\in\mathcal{F}_c} \frac{|\underline{S}_f|}{d_{c\tilde{c}}}. \tag{B8}$$

$\forall c, \tilde{c}, \in \{1, \dots, N_{cell}\}$ with $c \neq \tilde{c}$, the off-diagonal coefficients are

$$A_{c\tilde{c}} = -\theta\ \Delta t \frac{|\underline{S}_f|}{d_{c\tilde{c}}}. \tag{B9}$$

Remark 3. If the initial temperature for all cells is positive, $d > 0$, c_v, λ, R_a, and Δt are positive, all the diagonal terms of the matrix $\underline{\underline{A}}$ are strictly positive. Moreover, all off-diagonal coefficients are negative or null. Moreover, the diagonal terms are strictly larger than the sum of the modulus of off-diagonal terms. Therefore, A is diagonal dominant and a M-matrix. If for all cells c, B_c is strictly positive, then the solution of the linear system $\underline{X}$ is positive.

The right hand side terms B_c are strictly positive if:

$$\frac{\rho_c^n\Omega_c^n}{\Delta t} - \sum_{f\in\mathcal{F}_c}\left\langle\Theta\left(\rho^n,\ \rho^{n+1,k-1}\right)\underline{\tilde{u}}^k + \Delta t\underline{\nabla}p|_{n-1+\theta}^{n+\theta,k-1}\right\rangle_f \cdot \underline{S}_f + (1-\theta)\Delta t\sum_{f\in\mathcal{F}_c}\underline{\nabla}_f p|_{n-2+\theta}^{n-1+\theta}\cdot\underline{S}_f > 0, \tag{B10}$$

$$\Leftrightarrow CFL_p^+ < 1, \quad \text{where } CFL_p^+ \coloneqq \frac{\Delta t}{\rho_c^n\Omega_c^n}\sum_{f\in\mathcal{F}_c} a_f^\phi, \tag{B11}$$

and

$$a_f^\phi = \left\langle\Theta\left(\rho^n,\ \rho^{n+1,k-1}\right)\underline{\tilde{u}}^k + \Delta t\underline{\nabla}p|_{n-1+\theta}^{n+\theta,k-1}\right\rangle_f \cdot \underline{S}_f - (1-\theta)\Delta t\underline{\nabla}_f p|_{n-2+\theta}^{n-1+\theta}\cdot\underline{S}_f.$$

APPENDIX C. VARIABLE TIME STEP

In case of variable time step, some equations presented in Section 2.4 change. In the initialization step, $\underline{q}_f\Big|_n^{n+1,0}\cdot\underline{S}_f = \frac{\Delta t|_{n-1}^n}{\Delta t|_n^{n+1}}\underline{q}_f\Big|_{n-1}^n\cdot\underline{S}_f$. In the buoyant step, the discretized equations read:

$$\begin{aligned}
&\text{(a):}\ \frac{\rho_c^{n+1,k-1}Y_c^{n+1,k} - \rho_c^{n,k-1}Y_c^n}{\Delta t|_n^{n+1}} + \mathrm{Div}_c\left(\left\langle\Theta\left(Y^n,\ Y^{n+1,k}\right)\right\rangle_f \underline{q}_f\Big|_n^{n+1,k-1}\right) = \mathrm{Lap}_c\left(K, \Theta\left(Y^n,\ Y^{n+1,k}\right)\right), \text{for scalars,}\\
&\text{(b):}\ c_v\left[\frac{\rho_c^{n+1,k-1}T_c^{n+1,k} - \rho_c^{n,k-1}T_c^n}{\Delta t|_n^{n+1}} + \mathrm{Div}_c\left(\left\langle\Theta\left(T^n,\ T^{n+1,k}\right)\right\rangle_f \underline{q}_f\Big|_n^{n+1,k-1}\right)\right] = \Omega_c\mu(S_c^2)^{n+\theta} + \Gamma_c^{u^2/2}\Big|_n^{n+1,k-1}\\
&+ \mathrm{Lap}_c\left(\lambda, \Theta\left(T^n,\ T^{n+1,k}\right)\right) - \mathrm{Div}_c\left(\left\langle\Theta\left(p^n,\ p^{n+1,k-1}\right)\underline{u}^{n+\theta,k-1}\right\rangle_f\right) + \Omega_c\underline{u}_c^{n+\theta,k-1}\cdot\underline{\nabla}_c p|_{n-1+\theta}^{n+\theta,k-1}, \text{for temperature.}
\end{aligned} \tag{C1}$$

The corresponding kinetic energy source terms expression is modified as well:

$$\begin{aligned}
\frac{\Delta t|_n^{n+1}}{\Delta t|_{n-1+\theta}^{n+\theta}}\Gamma_c^{u^2/2}\Big|_n^{n+1,k-1} &= \left[1 - \frac{\Theta\left(\rho_c^n,\ \rho_c^{n+1,k-2}\right)}{\Theta\left(\rho_c^n,\ \rho_c^{n+1,k-1}\right)}\right]\left[\Theta\left(\rho_c^{n-1},\ \rho_c^n\right)\frac{|\underline{u}_c^{n-1+\theta}|^2}{2\,\Delta t|_{n-1+\theta}^{n+\theta}} - \mathrm{Div}_c\left(\frac{\left|\left\langle\Theta\left(\underline{u}^{n-1+\theta},\ \underline{\tilde{u}}^{k-1}\right)\right\rangle_f\right|^2}{2}\underline{q}_f\Big|_{n-1+\theta}^{n+\theta,k-2}\right)\right]\\
&- \frac{\Theta\left(\rho_c^n,\ \rho_c^{n+1,k-2}\right)}{\Theta\left(\rho_c^n,\ \rho_c^{n+1,k-1}\right)}\mathrm{Div}_c\left(\frac{\left|\left\langle\Theta\left(\underline{u}^{n-1+\theta},\ \underline{\tilde{u}}^{k-1}\right)\right\rangle_f - \underline{u}_c^{k-1}\right|^2}{2}\underline{q}_f\Big|_{n-1+\theta}^{n+\theta,k-2}\right) + \frac{\Theta\left(\rho_c^n,\ \rho_c^{n+1,k-2}\right)}{\Theta\left(\rho_c^n,\ \rho_c^{n+1,k-1}\right)}\Theta\left(\rho_c^{n-1},\ \rho_c^n\right)\frac{\left[|\underline{u}_c^{k-1} - \underline{u}_c^{n-1+\theta}|^2\right]}{2\,\Delta t|_{n-1+\theta}^{n+\theta}}.
\end{aligned} \tag{C2}$$

10970363, 2022, 12, Downloaded from https://onlinelibrary.wiley.com/doi/10.1002/fld.5116 by Jozef Stefan Institute, Wiley Online Library on [07/04/2025]. See the Terms and Conditions (https://onlinelibrary.wiley.com/terms-and-conditions) on Wiley Online Library for rules of use; OA articles are governed by the applicable Creative Commons License

The mass flux $\underline{q}_f\Big|_{n-1+\theta\ f}^{n+\theta,k-1}$ is defined by $\underline{q}_f\Big|_{n-1+\theta}^{n+\theta,k-1} = \Theta\left(\frac{\Delta t|_{n-1}^{n}}{\Delta t|_{n-1+\theta}^{n+\theta}}\underline{q}_f\Big|_{n-1}^{n}, \frac{\Delta t|_{n}^{n+1}}{\Delta t|_{n-1+\theta}^{n+\theta}}\underline{q}_f\Big|_{n}^{n+1,k-1}\right)$. The prediction step reads:

$$\frac{\Theta\left(\rho_c^n, \rho_c^{n+1,k-1}\right)\underline{\tilde{u}}_c^k - \Theta\left(\rho_c^{n-1}, \rho_c^{n,k-1}\right)\underline{u}_c^{n-1+\theta}}{\Delta t|_{n-1+\theta}^{n+\theta}} + \mathrm{Div}_c\left(\left\langle\Theta\left(\underline{u}^{n-1+\theta}, \underline{\tilde{u}}^k\right)\right\rangle_f \otimes \underline{q}_f\Big|_{n-1+\theta}^{n+\theta,k-1}\right) = -\underline{\mathrm{Grad}}_c\left(\left\langle p|_{n-1+\theta}^{n+\theta,k-1}\right\rangle_f\right) + \mathrm{Div}_c\left(\underline{\tau}_f^k\right) + \underline{f}_c\Big|_{n-1+\theta}^{n+\theta,k-1}. \tag{C3}$$

Moreover, the Helmholtz equation (13) turns into:

$$\frac{\rho_c^{n+1,k} - \rho_c^n}{\Delta t|_n^{n+1}} - \theta\mathrm{Lap}_c\left(\tau|_{n-1+\theta}^{n+\theta}, p^{n+1,k}\right) = -\mathrm{Div}_c\left(\left\langle\Theta\left(\rho^n, \rho^{n+1,k-1}\right)\underline{\tilde{u}}^k + \Delta t|_{n-1+\theta}^{n+\theta}\left(\underline{\nabla} p|_{n-1+\theta}^{n+\theta,k-1} + \delta\underline{f}^k\right)\right\rangle_f\right) + (1-\theta)\mathrm{Lap}_c\left(\frac{\Delta t|_n^{n+1}}{\Delta t|_{n-1}^{n}}\tau|_{n-1+\theta}^{n+\theta}, p|_{n-2+\theta}^{n-1+\theta}\right). \tag{C4}$$

where $\left(1-(1-\theta)\left(1-\frac{\Delta t|_n^{n+1}}{\Delta t|_{n-1}^{n}}\right)\right)\tau|_{n-1+\theta}^{n+\theta} = \Delta t|_{n-1+\theta}^{n+\theta}$. Finally, the expression (14) becomes:

$$\phi_c^k = \frac{\Theta\left(\frac{\Delta t|_n^{n+1}}{\Delta t|_{n-1}^{n}} p_c|_{n-2+\theta}^{n-1+\theta}, p_c^{n+1,k}\right)}{\left(1-(1-\theta)\left(1-\frac{\Delta t|_n^{n+1}}{\Delta t|_{n-1}^{n}}\right)\right)} - p_c|_{n-1+\theta}^{n+\theta,k-1}. \tag{C5}$$

10970363, 2022, 12, Downloaded from https://onlinelibrary.wiley.com/doi/10.1002/fld.5116 by Jozef Stefan Institute, Wiley Online Library on [07/04/2025]. See the Terms and Conditions (https://onlinelibrary.wiley.com/terms-and-conditions) on Wiley Online Library for rules of use; OA articles are governed by the applicable Creative Commons License